ISTANBUL TECHNICAL UNIVERSITY ★ GRADUATE SCHOOL

A STATISTICAL FRAMEWORK FOR FALSE-FIX ELIMINATION IN TERCOM USING REAL FLIGHT TEST DATA

M.Sc. THESIS

İbrahim Enes USLU

Department of Electronic and Communication Engineering

Telecommunications Engineering Programme

JANUARY 2026

ISTANBUL TECHNICAL UNIVERSITY ★ GRADUATE SCHOOL

A STATISTICAL FRAMEWORK FOR FALSE-FIX ELIMINATION IN TERCOM USING REAL FLIGHT TEST DATA

M.Sc. THESIS

İbrahim Enes USLU
(504221336)

Department of Electronic and Communication Engineering

Telecommunications Engineering Programme

Thesis Advisor: Assoc. Prof. Dr. Mehmet Nuri AKINCI

JANUARY 2026

İSTANBUL TEKNİK ÜNİVERSİTESİ ★ LİSANSÜSTÜ EĞİTİM ENSTİTÜSÜ

GERÇEK UÇUŞ TEST VERİLERİNİ KULLANARAK TERCOM’DA YANLIŞ KONUM KESTİRİMLERİNİN İSTATİSTİKSEL BİR ÇERÇEVE İLE ELENMESİ

YÜKSEK LİSANS TEZİ

İbrahim Enes USLU
(504221336)

Elektronik ve Haberleşme Mühendisliği Anabilim Dalı

Telekomünikasyon Mühendisliği Programı

Tez Danışmanı: Doç. Dr. Mehmet Nuri AKINCI

OCAK 2026

İbrahim Enes USLU, a M.Sc. student of ITU Graduate School student ID 504221336 successfully defended the thesis entitled “A STATISTICAL FRAMEWORK FOR FALSE-FIX ELIMINATION IN TERCOM USING REAL FLIGHT TEST DATA”, which he/she prepared after fulfilling the requirements specified in the associated legislations, before the jury whose signatures are below.

Thesis Advisor :	**Assoc. Prof. Dr. Mehmet Nuri AKINCI** Istanbul Technical University	....
Jury Members :	**Assist. Prof. Dr. Onur KURT** Istanbul Technical University	....
	Assist. Prof. Dr. Egemen BILGIN MEF University	....
		....

Date of Submission : **5 January 2026**
Date of Defense : **26 January 2026**

To my family,

FOREWORD

I would like to express my sincere gratitude to my advisor, Assoc. Prof. Dr. Mehmet Nuri Akıncı, for guiding me through every stage of this thesis with his knowledge and experience. His academic expertise and support throughout the process were invaluable in the preparation and development of this work.

I would also like to thank my colleague from TAI, Bilgehan Tanyeri, for generously sharing his experience and technical knowledge and providing all kinds of assistance. Furthermore, I thank Ümit Can Bekar PhD. for his valuable contributions and constructive guidance throughout this process.

Finally, I would like to extend my deepest gratitude to my dear family for their patience, moral support, and constant presence throughout the entire process.

January 2026 İbrahim Enes USLU

TABLE OF CONTENTS

ABBREVIATIONS

AUC	: Area Under the Curve
B/G	: Bad-to-Good Ratio
CFIT	: Controlled Flight Into Terrain
DBTC	: Database Terrain Cueing
DTED	: Digital Terrain Elevation Data
DTW	: Dynamic Time Warping
DTS	: Digital Terrain System
EKF	: Extended Kalman Filter
FFT	: Fast Fourier Transform
FTI	: Flight Test Instrumentation
GNSS	: Global Navigation Satellite System
IMU	: Inertial Measurement Unit
INS	: Inertial Navigation System
MAD	: Mean Absolute Difference
MI	: Mutual Information
MSD	: Mean Squared Difference
mRMR	: Minimum Redundancy Maximum Relevance
NCC	: Normalized Cross-Correlation
PGCAS	: Predictive Ground Collision Avoidance System
ROC	: Receiver Operating Characteristic
TERCOM	: Terrain Contour Matching
TRN	: Terrain-Referenced Navigation
UKF	: Unscented Kalman Filter

SYMBOLS

x	: Position vector
$\hat{x}$	: Estimated position vector
Δx	: Position error
h_i	: ith terrain height measurement
$\bar{h}$	: Mean terrain height
$z(x,y)$	: Digital terrain elevation
N	: Number of samples
σ_T	: Trajectory roughness (height standard deviation)
σ_Z	: Roughness difference (slope standard deviation)
$C_k(x)$	: TERCOM score map of metric k
$S(x)$	: Score map value
$S_{\min}$	: Minimum score (best match)
$S_{\mathbf{second}}$	: Second-best non-adjacent minimum
R_k	: Minima ratio of metric k
μ	: Mean value
σ^2	: Variance
H	: Entropy
Q_{25}, Q_{75}	: First and third quartiles
$P(f)$	: Spectral power
C	: Spectral centroid

LIST OF TABLES

LIST OF FIGURES

A STATISTICAL FRAMEWORK FOR FALSE-FIX ELIMINATION IN TERCOM USING REAL FLIGHT TEST DATA

SUMMARY

Terrain-Referenced Navigation (TRN) has been considered as a feasible alternative navigation method for aircraft operating in Global Navigation Satellite System (GNSS) denied environments. Terrain contour matching (TERCOM), a method based on the correlation between measured elevation profiles and stored digital terrain elevation data (DTED), is one of the most traditional TRN techniques. Despite its operational simplicity and proven applicability, TERCOM is inevitably susceptible to false-fix errors, where an incorrect terrain match is selected as the navigation solution. When these errors are transmitted to navigation systems, serious errors occur in situational awareness systems, and flight reliability decreases.

This thesis presents a statistical framework for identifying and eliminating errors that may be encountered in TERCOM. To do this, the core working logic of TERCOM is not altered; instead, a classification is performed using features generated during matching. First, a set of information-carrying features is identified, and then the candidate navigation solution is classified according to its relationship with this information. This method ensures that if a candidate navigation solution is considered unreliable, it is not transmitted to the navigation system.

This study is based on synthetic data generated from real Flight Test Instrumentation (FTI) recordings of the Hürjet, an advanced jet training aircraft. These recordings allow for the production of repeatable data while preserving realistic dynamics. A total of 780 different trajectories were generated. For each trajectory, six different metrics were examined: mean absolute difference (MAD), mean squared difference (MSD), normalized cross-correlation (NCC), dynamic time warping (DTW), mutual information (MI), and roughness-oriented comparison. The tests revealed that MAD and DTW have complementary characteristics.

To assess the reliability of the TERCOM solution, a total of forty-five candidate features were first extracted in three different contexts: trajectory-based, terrain map-based, and score map-based. These contexts respectively encompassed the characteristics of the altitude measurement sequence, the characteristics of the terrain map, and the characteristics of the values generated during matching. Then, feature elimination was performed using correlation analysis, mutual information ranking, receiver operating characteristic evaluation, and minimum redundancy–maximum relevance criteria methods. As a result of the elimination process, the minima-ratio, the ratio of the two lowest scores in the score map, emerged as the most distinctive feature. Roughness and roughness difference features were also added as auxiliary features.

A confidence-based elimination strategy was developed based on these indicators. The framework chooses between MAD and DTW position solutions according to their minima ratios. Then, utilizes threshold-based decisions to mitigate unreliable fixes. The experimental results indicate that the proposed framework maintains overall navigation accuracy while achieving a reduction in false-fix occurrences by 44%. The validation with actual flight test data provides the practical evidence of the approach.

This thesis illustrates that a statistical reliability assessment can significantly improve the robustness of TERCOM while causing minimal computational costs. The proposed framework offers a practical safeguard for TRN systems, enhancing operational safety in GNSS-denied environments.

GERÇEK UÇUŞ TEST VERİLERİNİ KULLANARAK TERCOM'DA YANLIŞ KONUM KESTİRİMLERİNİN İSTATİSTİKSEL BİR ÇERÇEVE İLE ELENMESİ

ÖZET

Arazi Referanslı Navigasyon (Terrain-Referenced Navigation, TRN), Küresel Konumlama Sistemi (Global Navigation Satellite System, GNSS) sinyallerinin karartıldığı, bozunduğu veya güvenilirliğinin azaldığı ortamlarda hava araçları için kritik bir alternatif navigasyon çözümü sunmaktadır. Özellikle askeri ve güvenlik odaklı görevlerde, GNSS'in kasıtlı karıştırma (jamming) ve aldatma (spoofing) tehditlerine açık olması, GNSS'e bağımlı sistemlerin tek başına yeterli olmasını engellemektedir. Bu nedenle, GNSS'ten bağımsız veya GNSS destekli ancak ona alternatif oluşturabilecek yöntemlerin geliştirilmesi büyük önem taşımaktadır.

TRN yöntemleri arasında Arazi Kontur Eşleştirme (Terrain Contour Matching, TERCOM), radar altimetre ölçümlerinin sayısal arazi yükseklik verileri (Digital Terrain Elevation Data, DTED) ile karşılaştırılmasına dayanan, hesaplama yükü görece düşük ve uzun yıllardır operasyonel olarak kullanılan bir yöntemdir. TERCOM algoritması, ölçülen yükseklik profillerini çevredeki olası konumlar üzerinde kaydırarak bir benzerlik haritası (skor haritası) üretir ve bu haritanın minimum noktasını en olası konum kestirimi olarak seçer. Bu yaklaşım, basitliği ve gerçek zamanlı uygulanabilirliği sayesinde pek çok hava ve deniz platformunda tercih edilmektedir.

Bununla birlikte, TERCOM algoritmasının en önemli zayıflıklarından biri, yanlış arazi eşleşmelerine dayalı olarak üretilen hatalı konum çözümleri, yani false-fix durumlarıdır. Özellikle düz veya düşük engebeli arazilerde, benzer yükseklik profillerinin birden fazla konumda ortaya çıkması, skor haritasında birden fazla güçlü minimum oluşmasına neden olabilmektedir. Bu durumda algoritma, gerçek konumdan çok uzak bir noktayı en iyi eşleşme olarak seçebilmektedir. False-fix hataları, entegre navigasyon sistemlerinde zincirleme etkilere yol açarak filtrelerin kararsızlaşmasına, durumsal farkındalığın azalmasına ve nihayetinde uçuş güvenliğinin ciddi şekilde tehlikeye girmesine neden olabilmektedir.

Literatürde, false-fix problemini azaltmaya yönelik çeşitli yaklaşımlar önerilmiştir. Bu yaklaşımlar genellikle benzerlik ölçütlerinin değiştirilmesi, adaptif pencereleme, filtre tabanlı yöntemler (EKF, UKF, parçacık filtreleri) veya yapay zekâ tabanlı modellerin kullanılması şeklinde sınıflandırılabilir. Ancak bu yöntemlerin büyük bir kısmı ya yüksek hesaplama maliyeti gerektirmekte ya da TERCOM'un temel çıktısının zaten güvenilir olduğu varsayımına dayanmaktadır. Oysa pratikte, filtrelerin güvensiz hale geldiği durumlarda başvurulan TERCOM çıktısının kendisi yanlış olduğunda, sistemin tamamı hatalı bir duruma sürüklenebilmektedir.

Bu tez çalışmasında, TERCOM algoritmasının temel eşleştirme mantığı değiştirilmeden, false-fix çözümlerinin tespit edilmesi ve elenmesine yönelik istatistik tabanlı bir

güvenilirlik çerçevesi önerilmektedir. Önerilen yaklaşım, yeni bir benzerlik metriği geliştirmekten veya ağır filtreleme yapıları eklemekten ziyade, TERCOM tarafından üretilen skor haritasının yapısal özelliklerinin analiz edilmesine odaklanmaktadır. Temel fikir, doğru bir konum çözümünün skor haritasında genellikle daha belirgin ve ayrışmış bir minimum ile temsil edildiği, yanlış çözümlerin ise birbirine yakın veya belirsiz minimumlar ürettiği varsayımına dayanmaktadır.

Çalışma kapsamında, Hürjet ileri seviye jet eğitim uçağından elde edilen gerçek Uçuş Test Enstrümantasyonu (Flight Test Instrumentation, FTI) verileri kullanılarak sentetik uçuş senaryoları oluşturulmuştur. Bu sentetik senaryolar, gerçekçi uçuş dinamiklerini korurken, kontrollü ve tekrarlanabilir istatistiksel analizlerin yapılmasına olanak tanımaktadır. Toplamda 780 farklı sentetik uçuş trajesi üzerinde altı farklı benzerlik metriği incelenmiştir: Ortalama Mutlak Fark (Mean Absolute Difference, MAD), Ortalama Kare Fark (Mean Squared Difference, MSD), Normalize Çapraz Korelasyon (NCC), Dinamik Zaman Bükme (Dynamic Time Warping, DTW), Karşılıklı Bilgi (Mutual Information, MI) ve pürüzlülük tabanlı karşılaştırma yöntemleri.

Yapılan kapsamlı deneysel analizler sonucunda, MAD ve DTW yöntemlerinin diğer metriklere kıyasla daha kararlı ve daha düşük hatalı sonuçlar ürettiği gözlemlenmiştir. Bununla birlikte, bu iki yöntemin her senaryoda aynı performansı göstermediği, bazı durumlarda birinin doğru konumu bulurken diğerinin false-fix üretebildiği tespit edilmiştir. Bu gözlem, farklı metriklerin arazi–ölçüm uyumunun farklı yönlerini yakaladığını ve birlikte kullanılmalarının potansiyel fayda sağlayabileceğini göstermektedir.

TERCOM çıktılarının güvenilirliğini değerlendirmek amacıyla, üç farklı kaynaktan toplam kırk beş aday özellik çıkarılmıştır: uçuş trajesine dayalı özellikler, sayısal arazi haritasına dayalı özellikler ve skor haritasına dayalı özellikler. Bu özellikler üzerinde korelasyon analizi, karşılıklı bilgi (mutual information), alıcı işletim karakteristiği (ROC) analizi ve minimum fazlalık–maksimum alaka (mRMR) yöntemlerini içeren çok aşamalı bir eleme süreci uygulanmıştır. Bu süreç sonucunda, skor haritasındaki en güçlü iki komşu olmayan minimum arasındaki ayrımı ölçen minima oranı (minima ratio) en güvenilir gösterge olarak belirlenmiştir. Buna ek olarak, uçuş trajesinin pürüzlülüğü (roughness) ve pürüzlülük farkı (roughness difference) da false-fix tespitinde önemli destekleyici göstergeler olarak öne çıkmıştır.

Belirlenen bu göstergeler kullanılarak, minima oranına dayalı bir metrik birleştirme ve eleme stratejisi geliştirilmiştir. Bu strateji kapsamında, MAD ve DTW skor haritaları karşılaştırılmakta ve daha belirgin minimum üreten metrik, o pencere için tercih edilmektedir. Ardından, minima oranı ve pürüzlülük tabanlı eşik testleri uygulanarak güvenilir olmayan çözümler abstain olarak işaretlenmekte ve navigasyon güncellemesine dahil edilmemektedir. Deneysel sonuçlar, önerilen yaklaşımın false-fix oranını %44'ten fazla azalttığını ve genel navigasyon doğruluğunu koruduğunu göstermektedir.

Bu tez çalışmasında önerilen yaklaşımın önemli bir avantajı, mevcut ataletsel seyrüsefer sistemleri ve hata-durumlu filtre mimarileri ile doğrudan uyumlu olmasıdır. Modern hava araçlarında yaygın olarak kullanılan hata-durumlu Kalman filtreleri, küçük ve kademeli düzeltmeler için tasarlanmıştır; ancak konum hatasının zamanla büyüdüğü ve kovaryansın aşırı arttığı durumlarda, filtre düzeltmelerinin etkisiz kaldığı bilinmektedir. Bu tür senaryolarda, TERCOM tabanlı mutlak konum kestirimleri filtre için kritik bir harici ölçüm kaynağı olarak kullanılmaktadır. Ancak TERCOM çıktısının güvenilir olmadığı bir durumda, bu ölçümün filtreye enjekte edilmesi, filtre ıraksamasına ve sistem kararsızlığına yol açabilmektedir. Bu bağlamda, tezde geliştirilen false-fix eleme çerçevesi, TERCOM'un filtreye sağladığı konum bilgisinin güvenilirliğini artırarak, entegre navigasyon mimarisinin genel kararlılığına doğrudan katkı sağlamaktadır.

Önerilen yöntemin bir diğer önemli özelliği, operasyonel uygulanabilirliğinin yüksek olmasıdır. Çalışmada kullanılan güvenilirlik göstergeleri, halihazırda TERCOM algoritması tarafından üretilen skor haritası ve radar altimetre ölçümleri üzerinden elde edilmekte olup, ek sensör veya yüksek hesaplama gücü gerektirmemektedir. Bu durum, yöntemin gerçek zamanlı sistemlerde, gömülü aviyonik donanımlar üzerinde uygulanmasını mümkün kılmaktadır. Ayrıca, önerilen eleme stratejisi deterministik bir yapıya sahip olduğundan, sertifikasyon süreçleri açısından da avantaj sunmaktadır. Bu özellikler, çalışmanın yalnızca akademik değil, aynı zamanda pratik ve operasyonel açıdan da değerli bir katkı sunduğunu göstermektedir. Tez kapsamında elde edilen sonuçlar, TERCOM tabanlı sistemlerin GNSS'in güvenilir olmadığı ortamlarda daha emniyetli ve tutarlı bir şekilde çalışmasına yönelik somut bir çözüm ortaya koymaktadır.

Gerçek uçuş test verileriyle yapılan doğrulama çalışmaları, yöntemin pratik uygulanabilirliğini ve operasyonel etkinliğini ortaya koymaktadır. Sonuç olarak, bu tez çalışması, düşük hesaplama maliyetli istatistiksel güvenilirlik analizlerinin TERCOM tabanlı navigasyon sistemlerinin dayanıklılığını anlamlı ölçüde artırabileceğini göstermektedir. Önerilen çerçeve, GNSS'in güvenilir olmadığı ortamlarda çalışan hava araçları için pratik ve etkili bir güvenlik katmanı sunmaktadır.

1. INTRODUCTION

Modern aviation, autonomous systems and defense applications depend on accurate and reliable navigation. Navigation in aircraft typically utilizes filtered data from the Inertial Navigation System (INS) and the Global Navigation Satellite System (GNSS). However, GNSS signals are vulnerable to intentional interference, spoofing, and jamming; therefore, being able to function in GNSS-denied environments becomes crucial. Terrain-referenced navigation (TRN) is a well-established alternative solution that uses the distinctive characteristics of the Earth's surface to estimate position without the use of GNSS signals. It performs this position estimation by matching measured earth-based features with digital terrain elevation data (DTED) stored on-board. Additionally, this position estimation can be used in modern Digital Terrain Systems (DTS) applications such as TERPROM®, which provides awareness for Controlled Flight Into Terrain (CFIT) situations and plays a critical role.

Modern Digital Terrain Systems (DTS) play a critical role in ensuring flight safety by providing situational awareness to the pilot in Controlled Flight into Terrain (CFIT) scenarios. CFIT situations are accidents that occur when the pilot is in control and the flight is typically at low altitude. Systems like DTS predict potential collisions in such situations through various algorithms and provide the pilot with the necessary warnings. Examples of these algorithms include the Predictive Collision Avoidance System (PGCAS), Obstacle Warning and Cuening (OWC), and Database Terrain Cuing (DBTC). PGCAS provides information and warnings about avoiding terrain, OWC about avoiding obstacles such as buildings and power poles, and DBTC about maintaining a specific altitude. These functions increase safety in low-altitude flights. In short, TRN (Traffic Navigation System) essentially offers both an alternative navigation solution for GNSS-denied environments and provides the positional information on the digital map necessary for DTS algorithms.

In current TRN (Terminal Navigation and Navigation) studies, navigation estimation is generally performed using filter-based approaches such as the extended Kalman filter (EKF) or the odorless Kalman filter (UKF). For various reasons, the uncertainties of these filters can increase over time, leading to a loss of confidence in the navigation solution. When the filter uncertainty exceeds a predetermined limit, the TERCOM algorithm is used. The position estimate obtained from TERCOM is fed into the filter, thus ensuring that the filter is stabilized and made reliable.

Based on these motivations, the present study applies an advanced version of the Terrain Contour Matching (TERCOM) algorithm to the Hürjet, an advanced jet training aircraft shown in Figure 1.1. The aim is to improve TRN accuracy by detecting and eliminating false-fix events encountered in TERCOM, thereby increasing operational reliability.

Figure 1.1: Hürjet in-flight image (adapted from Turkish Aerospace official website).

The TERCOM algorithm compares a radar-altimeter (radalt) sequence against a stored DTED by sliding the measured profile over candidate locations to form a score map. Each pixel denotes a candidate position; lower scores indicate better matches. The minimum of this surface corresponds to the best match, which is then selected as the navigation fix. This simple yet powerful idea has enabled robust operation in GNSS-denied conditions and has been successfully applied in various airborne and maritime systems.

Even though TERCOM is useful, it can find incorrect matches, which lead to *false fixes*. The main reasons for encountering the incorrect matches can be expressed as follows: the roughness of the terrain being flown over is not unique, the loss of data is caused by the discretization of the flight profile, and the corruption of the digital terrain database and radar altimeter by random noise. These phenomenons drive the navigation solution into an erroneous state. The most critical problem here is that detecting these false matches is inherently difficult. Previous works have attempted to improve potential fixes by modifying similarity measures (e.g., MAD, MSD, NCC) or embedding TERCOM within more sophisticated filters (e.g., particle filters). Although such approaches can enhance overall performance, they remain dependent on the reliability of the underlying TERCOM output. In practice, when the filter loses reliability, it uses TERCOM-based corrections to restore that reliability. Therefore, if TERCOM itself provides an incorrect correction, the entire navigation solution can go astray. For this reason, the issue of incorrect correction detection within TERCOM is a problem that needs to be addressed.

This study analyzes the features generated during the matching calculation, instead of redesigning the matching algorithm in TERCOM or using complex filters. Distinguishing features are identified from the obtained statistical features and used in the decision-making mechanism. The proposed framework identifies unreliable incoming measurements and prevents their inclusion in the navigation process. This method reduces the number of false fixes without significantly increasing the computational load. The robustness and operational applicability of the method were tested using datasets created from Flight Test Instrumentation (FTI) recordings obtained from Hürjet flight tests.

2. LITERATURE REVIEW

A wide spectrum of TRN techniques has been investigated. TERCOM is the most well-known method, originally deployed in cruise missiles [2] and continues to serve as the baseline for TRN studies. Since its introduction in the 1980s, TRN research has evolved through three main phases. The first one is correlation-based acquisition algorithms as TERCOM and Digital Scene Matching Area Correlator (DSMAC) [3] . The second one is filter-based sequential tracking algorithms such as SITAN [4]–[6] and EKF/UKF/PF based approaches [7]–[13]. The last one is hybrid approaches combining TERCOM-based acquisition and SITAN-style tracking [11,14]–[16]. Hybrid approaches demonstrate improved robustness at the cost of computational complexity. Additionally, modern DTS's uses hybrid approaches such as TERPROM® [17] to provide situational awareness.

Building on these foundations, several studies improved the TERCOM algorithm by using new similarity metrics such as mean absolute difference (MAD), mean squared difference (MSD), and normalized correlation [18,19]. Adaptive window sizing, iterative matching, and entropy-based terrain selection improved distinctiveness and robustness, but did not eliminate false matches in smooth terrain [20]. Other implementations focused on system-level integration for terrain-aided navigation [21,22], showing practical feasibility on embedded platforms.

In recent years, AI-based methods have been investigated to enhance TRN performance. Neural networks, including recurrent architectures, have been applied for sequence-to-location estimation [23], while CNN- and GAN-based approaches have improved digital elevation model (DEM) consistency and terrain representation. PCNN-based similarity measures improved nonlinear terrain matching [24,25]. In previous work by our team, AI-assisted digital terrain systems [26] with adaptive models were introduced. In other study, our team conducted a validation study using real FTI data [1] proving that AI-supervised filtering and adaptive mode switching can achieve reliable under actual flight conditions.

Several researchers have directly focused on mitigating the false-fix problem. A mismatch diagnostic for underwater gravity-aided TERCOM [27] implemented spatial order constraints to eleminate inconsistent matches, while confidence-assessment frameworks [28] estimated reliability scores correlated with true error. Multi-metric voting [11] and terrain suitability analyses [29,30] reduced false fixes by accepting updates only when multiple criteria agreed. Domain-mismatch suppression models [31,32] further minimized spurious minimas. However, most works deal with false fixes indirectly, relying on filter consistency or auxiliary cues rather than explicit diagnostics. Past studies are categorized in Table 2.1 according to their false-fix handling strategy.

Table 2.1: Survey of false-fix handling approaches in TRN literature.

Category	Reference IDs	Notes
False fixes not discussed	[3,15]–[17], [22,23,25]	Focus on correlation or efficiency; false-fix issue not analyzed.
False fixes stated as a problem	[2,14,21]	Acknowledge false fixes as a limitation in low-relief terrain but offer no mitigation.
False fixes indirectly improved	[1,5]–[10,12,13], [18,19,24,26]	Adaptive filtering or similarity refinements indirectly reduce mismatches.
False fixes directly addressed	[11,20,27]–[32]	Explicit diagnostics. RSOC diagnostics, confidence filtering, multi-metric voting, and entropy-based TERCOM.

In summary, TRN algorithms, originating from the TERCOM studies, have been enhanced over time by combining them with various filters and AI structures. Current TRN methods still rely on TERCOM as a baseline. Therefore, avoiding false-fixes or being able to predict them is crucial. Research on false-fix prediction in the literature is deficient on low computing demands, ease of implementation, and testing with FTI data for demonstrating its consistency under real flight conditions. This research addresses the existing gap in the literature.

3. TERCOM AND STATISTICAL ANALYSIS

3.1 Terrain Server

The terrain server interprets DTED-2 elevation data to provide digital terrain models with a spatial resolution of 1 arc-second (∼30 m). The onboard database enables rapid access to elevation values for various query types, including height-of-terrain (HoT) and height-above-terrain (HaT). For HaT and HoT requests, the server returns the terrain elevation either for a single point or for a $V \times V$ matrix centered at a specified location. The matrix center is given in latitude and longitude degrees, and in this study, the matrix configuration of the terrain server was mainly used. Further details of terrain server can be found in [1,26].

Fig. 3.1 illustrates the geometric relationship between barometric, radalt and DTED heights. h_{baro} denotes the aircraft's altitude, h_{radalt} is the radar altimeter reading, and h_{DTED} corresponds to terrain height from the server. Accordingly, $h_{baro} - h_{radalt}$ represents the estimated terrain elevation, which is directly compared to h_{DTED} in the TERCOM algorithm by minimizing the difference between these sequences.

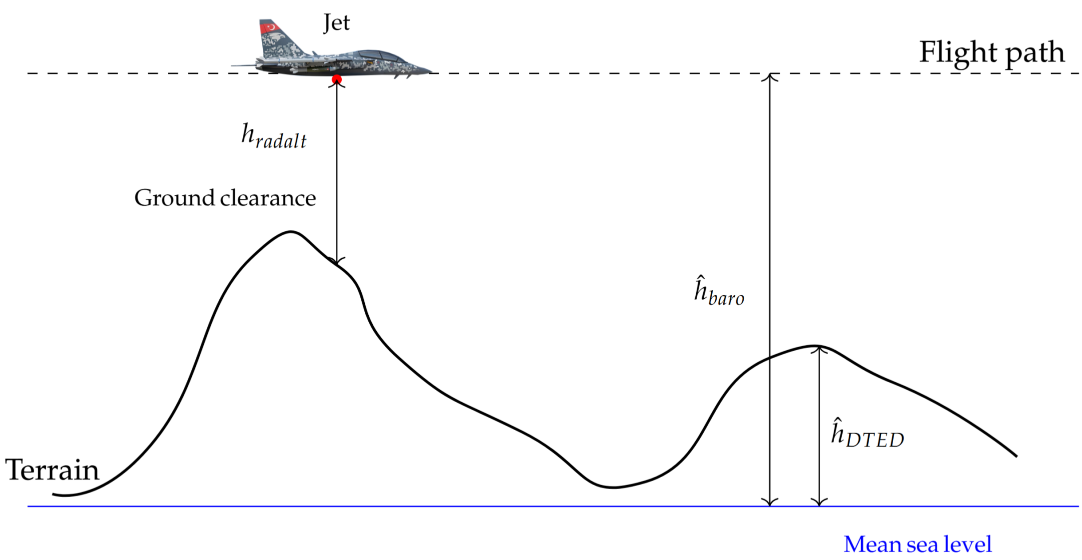

Figure 3.1: Measurement geometry of barometric, radalt, and DTED heights from [1].

3.2 Traditional TERCOM

TERCOM is a matching technique for finding the position of the aircraft with respect to the terrain of the surrounding area. The comparison is made between the terrain elevation profile in the form of relative motion obtained from the terrain around the aircraft's estimated position and the terrain elevation sequence measured from the radar altimeter. The starting point of this relative motion is shifted across the surrounding terrain map, and this comparison process is repeated, and the most similar result is accepted as the algorithm output. Algorithm overview is given in Fig. 3.2.

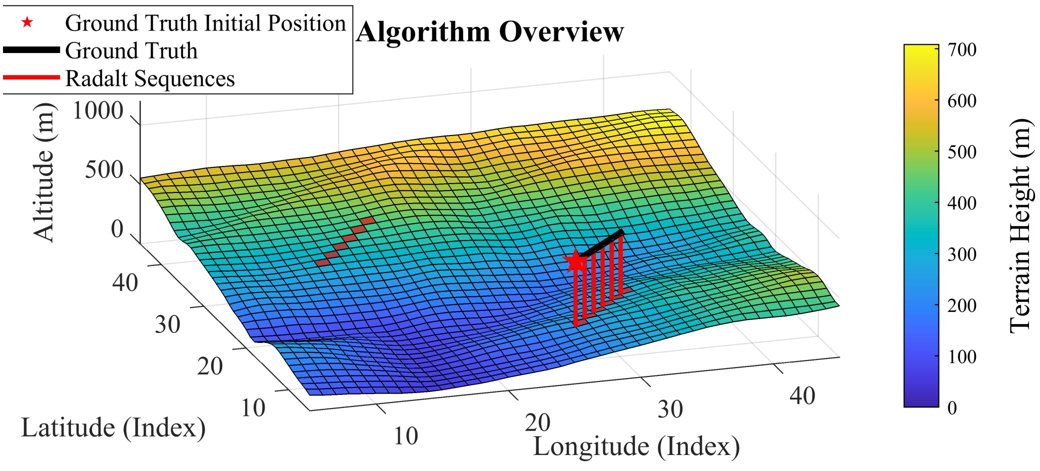

Figure 3.2: TERCOM algorithm overview.

The terrain data is stored as a VxV matrix in the onboard computer. To perform the mathcing and determine the aircraft location relative to the terrain, following algorithm is used:

$$x, y = \underset{x,y}{\operatorname{argmin}} f(x, y) \tag{3.1}$$

Where x and y are all possible locations of the first measurement relative to the terrain matrix. It is the location of the aircraft within the terrain elevation matrix. From these values, the aircraft location can be predicted. The function f can be defined as follows:

$$f(x, y) = \sum_{i=1}^{N} g(h_i, H_{x+x_{h_i}, y+y_{h_i}}) \tag{3.2}$$

The h is the measured profiles of the aircraft using the radalt, and the H is the terrain matrix stored in the onboard computer. For every profile, its measured terrain height and the stored height are compared using a comparison function g. The inputs to the comparison function x_{h_i}, y_{h_i} is the relative position of the current profile to the first measurement in the current measurement window. In our case, the comparison function $g(x)$ is the mean absolute distance (MAD), which can be defined as follows:

$$g(x,y) = |x - y| \tag{3.3}$$

Therefore, our algorithm chooses the starting location of the current aircraft path which has the most similar terrain height profile relative to the stored heights. Then, the current location (the end point of the path) is calculated.

3.3 Sample Count (N)

TERCOM uses N samples during matching. As N increases, the accuracy of the navigation solution improves. As seen in Fig. 3.3, which was created by experiments using MAD and different N values, the mean error and the standard deviation decrease. However, as the number of sample counts increases, the computational load also increases, and it would be more appropriate to determine this number based on hardware capabilities. Therefore, in this study, the sample count is not considered and N = 40 is set as a constant, corresponding to a 2-second data sequence for a system operating at 20 Hz.

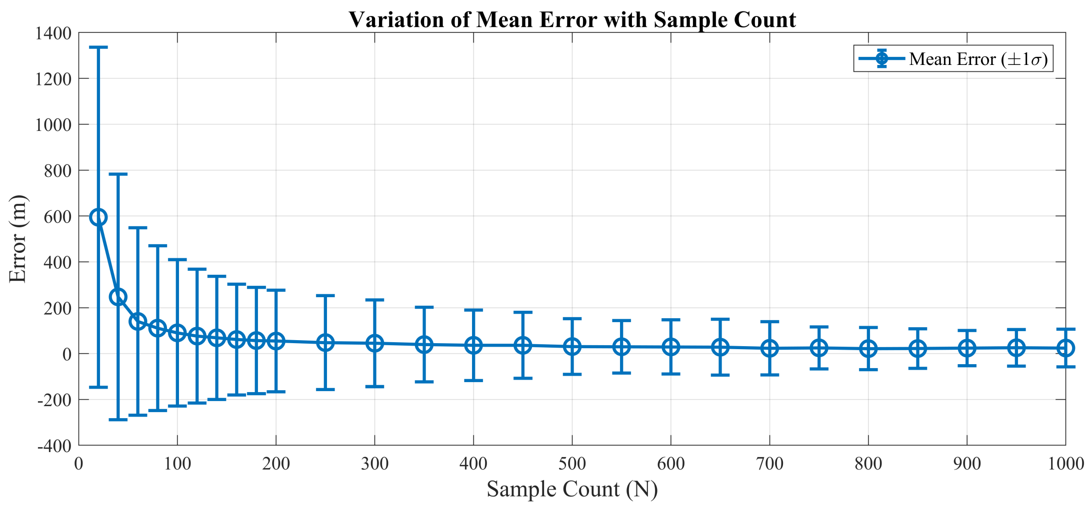

Figure 3.3: Navigation error comparisons for different sample counts.

3.4 Matching Metrics

The foundation of the proposed approach is the construction of score maps that quantify the similarity between measured terrain profiles and map-derived profiles. For each candidate position within the search area, function $f(x,y)$ is evaluated. Definition of h and H is the same as in the traditional TERCOM. Similar to formula 3.1, the minimum argument value of $f(x,y)$ yields the best match. $f(x,y)$ corresponds the result of the cost function $g(x,y)$ described in this section. For convenience with different functions, the summation operation for N measurements were included in the function $g(x,y)$.

$$f(x,y) = g(h, H_{x+x_h, y+y_h}) \tag{3.4}$$

To systematically assess which comparison function is most suitable for TERCOM correlation, sixsimilarity measures are investigated. These metrics capture different statistical perspectives on the relationship between the sequences.

3.4.1 Mean absolute difference (MAD)

MAD captures the average absolute difference between the measured and reference sequences and is robust to outliers.

$$\mathrm{MAD}(x,y) = \frac{1}{N}\sum_{i=1}^{N}|x_i - y_i| \tag{3.5}$$

3.4.2 Mean square difference (MSD)

MSD calculates the average squared difference between measured and reference sequences. It penalizes the large deviations due to the squared term.

$$\mathrm{MSD}(x,y) = \frac{1}{N}\sum_{i=1}^{N}(x_i - y_i)^2 \tag{3.6}$$

3.4.3 Normalized cross-correlation (NCC)

NCC measures the correlation strength between the centered sequences, normalized by their variance. Unadjusted normalized cross-correlation (UNCC) in formula 3.7 gives values close to 1 indicate strong similarity, whereas values near -1 indicate strong inverse similarity. UNCC values close to 0 indicates weak alignment. Due to this, transformation in formula 3.8 is utilized for lower scores close to 0 to indicate a better alignment.

$$\mathrm{UNCC}(x,y) = \frac{\sum_{i=1}^{N}(x_i - \bar{x})(y_i - \bar{y})}{\sqrt{\sum_{i=1}^{N}(x_i - \bar{x})^2 \sum_{i=1}^{N}(y_i - \bar{y})^2}} \tag{3.7}$$

$$\mathrm{NCC}(x,y) = -(|UNCC(x,y)| - 1) \tag{3.8}$$

3.4.4 Dynamic time warping (DTW)

DTW aligns the sequences by locally stretching or compressing one relative to the other, allowing non-linear temporal deformations, and minimizes the cumulative alignment distance over a monotonic and continuous warping path π, thereby accommodating local time shifts and small trajectory misalignments.

$$\mathrm{DTW}(x,y) = \min_{\pi \in \mathscr{A}(x,y)} \sum_{(i,j)\in\pi} \left| x_i - y_j \right| \tag{3.9}$$

3.4.5 Mutual information (MI)

MI quantifies the statistical dependence between x and y, based on their joint and marginal probability distributions. H(X) is the entropy of radalt sequence and I(X;Y) is the mutual information of radalt sequence and predicted sequences. Higher I(X;Y) indicates greater shared information, so by the transformation in formula 3.12 MI(x,y) becomes the function that gives the best match at low values close to 0.

$$\mathrm{H}(X) = -\sum_{x} p(x) \log_2 p(x) \tag{3.10}$$

$$\mathrm{I}(X;Y) = \sum_{x,y} p(x,y) \log_2 \frac{p(x,y)}{p(x)\,p(y)} \tag{3.11}$$

$$\mathrm{MI}(x,y) = H(X) - I(X;Y) \tag{3.12}$$

3.4.6 Roughness oriented comparison (ROC)

This method investigates the differences of height measurements instead of comparing height measurements directly. Three metrics, MAD, MSD and SGN are normalized and combined. For ROC calculation, in the MAD and MSD height differences used instead of heights. SGN is sign match of height differences. Due to difference operation $N-1$ samples occur instead of N and $norm(\cdot)$ denotes linear min–max normalization.

$$\Delta x_i = x_{i+1} - x_i \tag{3.13}$$

$$\Delta y_i = y_{i+1} - y_i \tag{3.14}$$

$$\mathrm{MAD_{ROC}}(x,y) = \frac{1}{N-1} \sum_{i=1}^{N-1} \left| \Delta x_i - \Delta y_i \right| \tag{3.15}$$

$$\mathrm{MSD_{ROC}}(x,y) = \frac{1}{N-1}\sum_{i=1}^{N-1}(\Delta x_i - \Delta y_i)^2 \tag{3.16}$$

$$\mathrm{SGN_{ROC}}(x,y) = \frac{1}{N-1}\sum_{i=1}^{N-1}(sign(\Delta x_i) == sign(\Delta y_i)) \tag{3.17}$$

$$\mathrm{ROC}(x,y) = 0.4 * norm(MAD_{ROC}) + 0.3 * norm(MSD_{ROC}) + 0.3 * norm(1 - SGN_{ROC}) \tag{3.18}$$

To evaluate these metrics in practice, each matching metric was applied to the FTI-derived datasets and used to compute position estimates across thousands of trials over 780 different trajectories described in Section 3.5. These trajectories span a wide range of terrain characteristics and flight segments, enabling a statistically meaningful comparison under diverse matching conditions. For each trial, the resulting navigation error was recorded and aggregated to form empirical error distributions. The resulting error distributions are shown in Fig. 3.4.

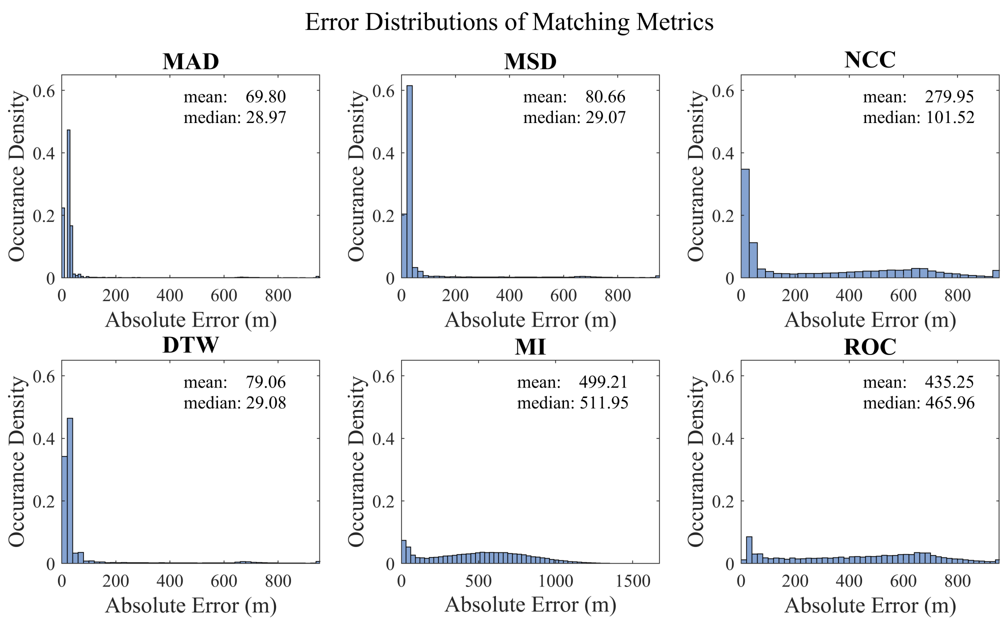

Figure 3.4: Navigation error comparisons of different matching metrics.

Among these six metrics, wide error histograms with long tails, indicating unstable behavior and frequent large errors were observed in NCC, MI, and ROC. The MSD and TKY metrics showed intermediate error results. MAD and DTW produced tight error distributions with low variance, so the choice between these two functions was deemed appropriate.

3.5 Feature Extraction

Statistical analysis uses synthetic data derived from real FTI logs, which keeps physical realism while supporting controlled conditions. Synthetic datasets were generated from recorded INS/GNSS channels, allowing the generation of repeatable test scenarios for algorithm development. The flight path being used for generating synthetic flights is illustrated in Fig. 3.5.

Under normal circumstances, generating such real data would be an impractical and expensive solution due to both logistical and operational costs. However, thanks to the synthetic data-generating framework, numerous flight conditions have been generated under countless different scenarios and can be used as ground truth. This allows for statistical analysis against all possible terrain types, and algorithm performance can be easily compared with real results.

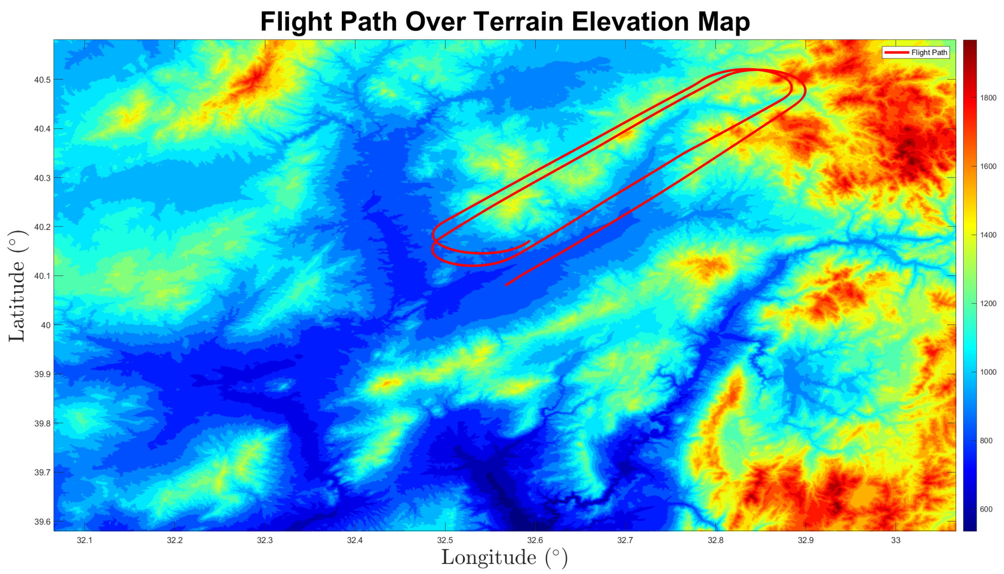

Figure 3.5: Actual flight path, from [1].

780 different flight paths given in Fig. 3.6 are created from the cropped wings-level flight part of the actual flight path. Synthetic radar altimeter measurements were obtained using the HaT function of the terrain server. Additive standard gaussian white noise was applied to these data.

The reliability of TERCOM can only be assessed if candidate navigation fixes are characterized by informative descriptors. In order to do this, 45 candidate features

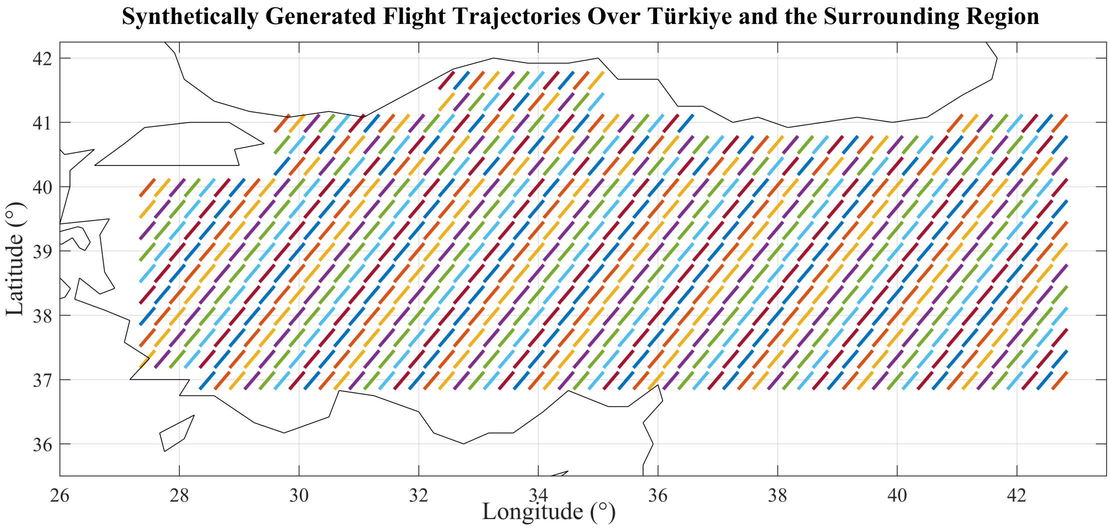

Figure 3.6: Synthetic flight paths over Türkiye and the surrounding region.

are systematically extracted from three complementary sources: (i) the radar altimeter trajectory itself, (ii) the underlying digital terrain map, and (iii) the resulting TERCOM score map. This multi-domain approach ensured that both input signals and algorithm outputs contributed to the reliability analysis. By jointly considering measurement variability, terrain distinctiveness, and score-map structure, the extracted features capture both the physical characteristics of the flight environment and the internal behavior of the matching process. Fig. 3.7 illustrates the feature extraction and decision-making schematic.

3.5.1 Trajectory-based features

The first group consists of features directly derived from the measured altitude sequence. These features include the trajectory roughness and the roughness difference. Smoother trajectories naturally offer fewer discriminative clues whereas highly varied sequences increase distinctiveness.

Sample count: Sample count refers to the number of altitude measurements used within a single matching window. It determines the temporal length of the terrain profile employed in the TERCOM correlation process. The effect of sample count on matching performance and computational load is analyzed in Section 3.3. In addition, sample count is excluded from this study.

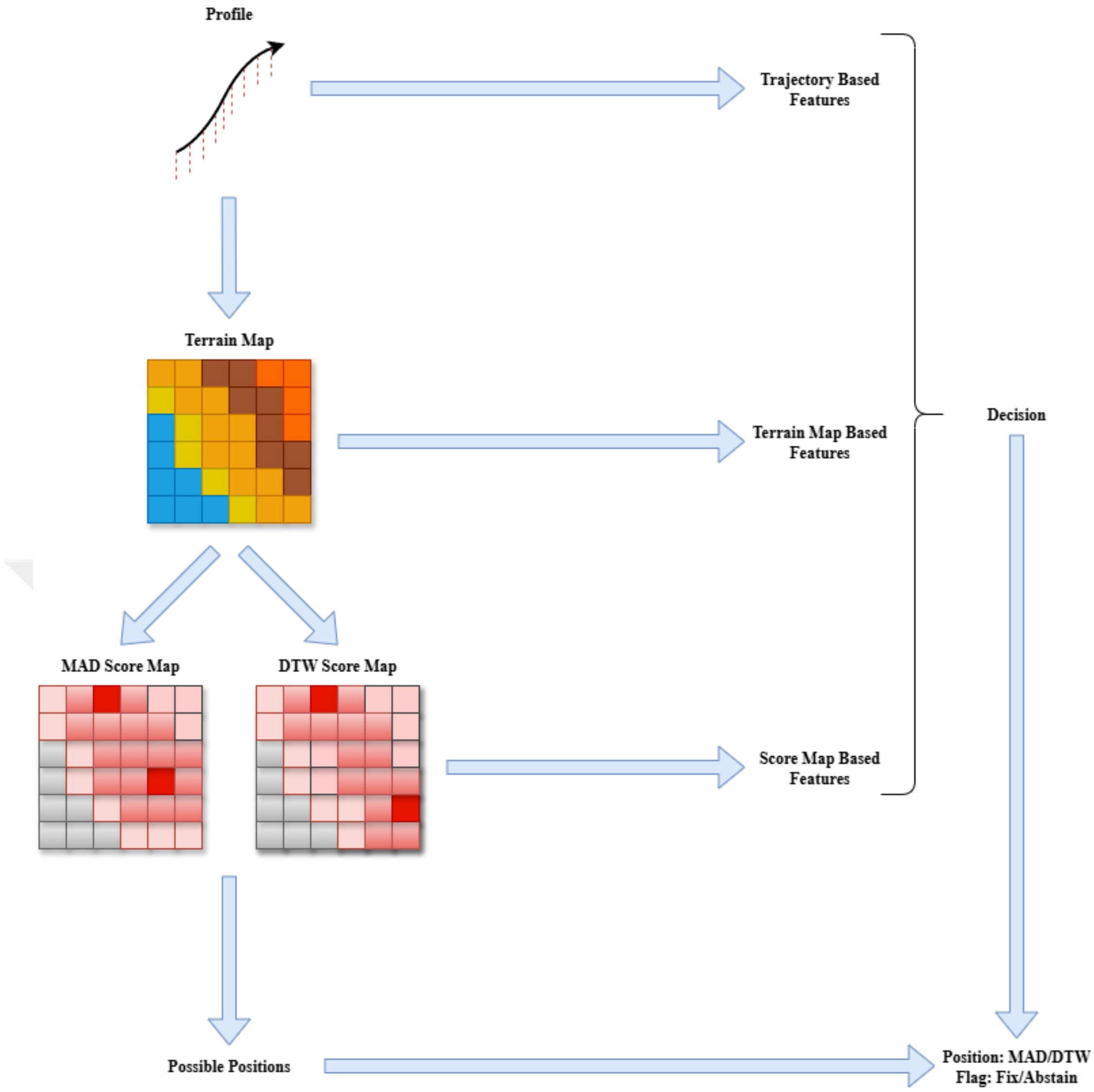

Figure 3.7: Feature extraction and decision making schematic.

Trajectory roughness: Trajectory roughness represents the standard deviation of the altitude sequence and quantifies the overall variability of the flight profile. Higher roughness generally increases terrain distinctiveness and improves matching reliability. The mathematical formulation and its impact on false-fix behavior are detailed in Section 4.5.

Trajectory roughness difference: Trajectory roughness difference measures the variability of consecutive altitude differences, capturing local slope fluctuations along the trajectory. This feature emphasizes rapid terrain changes and complements the roughness metric. Its definition and role in false-fix discrimination are discussed in Section 4.5.

3.5.2 Terrain map–based features

The second group captured structural properties of the map tiles retrieved from the DTED database. Standard geomorphological descriptors such as the terrain ruggedness index (TRI), topographic position index (TPI), slope and curvature statistics, skewness, kurtosis, height range, number of slopes and slope density were included. Frequency-domain (FFT) representations were also considered, including Fourier energy, power, bandwidth, entropy, and spectral centroid. These descriptors quantify the distinctiveness of the local terrain patch and are expected to influence the separability of candidate matches.

Terrain map mean terrain ruggedness index (TRI): The TRI quantifies local elevation variability by measuring the average absolute height difference between a grid cell and its neighbors, reflecting surface roughness.

$$\mathrm{TRI} = \frac{1}{N}\sum_{i=1}^{N} |z_i - \bar{z}| \tag{3.19}$$

Terrain map TRI ARS classification index: This feature represents a categorical ruggedness classification derived from TRI values, mapping continuous terrain roughness into discrete terrain classes.

$$\mathrm{TRI}_{\mathrm{class}} = \mathscr{C}(\mathrm{TRI}) \tag{3.20}$$

Terrain map mean topographic position index (TPI): TPI is used for identify ridges or valleys by measuring the elevation of a location relative to the surrounding area.

$$\mathrm{TPI} = z_0 - \frac{1}{N}\sum_{i=1}^{N} z_i \tag{3.21}$$

Terrain map TPI local elevation (TPI_{LE}): This feature measures the local elevation variation in relation to the adjacent terrain at a specified spatial scale.

$$\mathrm{TPI}_{\mathrm{LE}} = z_0 - \mu_{\mathrm{local}} \tag{3.22}$$

Terrain map TPI positive value sum (TPI_{PVS}): $\mathrm{TPI}_{\mathrm{PVS}}$ allows to highlight ridge-dominated terrain features with positive TPI values on the existing map.

$$\mathrm{TPI}_{\mathrm{PVS}} = \sum_{i=1}^{N} \max(\mathrm{TPI}_i, 0) \tag{3.23}$$

Terrain map maximum TPI: This feature indicates the maximum TPI value within the current terrain map. In other words, it highlights the most prominent topographic feature.

$$\mathrm{TPI}_{\max} = \max_i(\mathrm{TPI}_i) \tag{3.24}$$

Terrain map TPI surface area ratio (TPI_{SAR}): $\mathrm{TPI}_{\mathrm{SAR}}$ expresses the ratio of positively elevated terrain relative to the total map area.

$$\mathrm{TPI}_{\mathrm{SAR}} = \frac{N(\mathrm{TPI}_i > 0)}{N_{\mathrm{total}}} \tag{3.25}$$

Terrain map mean terrain slope: The mean slope measures the average gradient magnitude over the terrain tile, which shows how steep the terrain is generally.

$$\bar{s} = \frac{1}{N} \sum_{i=1}^{N} \sqrt{\left(\frac{\partial z}{\partial x}\right)^2 + \left(\frac{\partial z}{\partial y}\right)^2} \tag{3.26}$$

Terrain map mean planar curvature: Planar curvature is the curvature of land that is perpendicular to the slope direction and is related to flow divergence or convergence.

$$k_p = \frac{\partial^2 z}{\partial x^2} + \frac{\partial^2 z}{\partial y^2} \tag{3.27}$$

Terrain map mean profile curvature: Profile curvature measures curvature along the slope direction and influences acceleration or deceleration of flow.

$$k_{pr} = \frac{\partial^2 z}{\partial s^2} \tag{3.28}$$

Terrain map terrain height skewness: Skewness characterizes the asymmetry of elevation distribution within the terrain.

$$\mathrm{Skewness} = \frac{1}{N\sigma^3} \sum_{i=1}^{N} (z_i - \mu)^3 \tag{3.29}$$

Terrain map terrain height kurtosis: Kurtosis indicates the degree of peakedness in the elevation distribution.

$$\mathrm{Kurtosis} = \frac{1}{N\sigma^4} \sum_{i=1}^{N} (z_i - \mu)^4 \tag{3.30}$$

Terrain map entropy: Entropy quantifies the randomness of terrain elevation values, which reflects the unpredictability of the surface.

$$H = -\sum_k p_k \log p_k \tag{3.31}$$

Terrain map mean elevation: The terrain map mean elevation represents the average terrain height within the tile under consideration.

$$\mu = \frac{1}{N}\sum_{i=1}^{N} z_i \tag{3.32}$$

Terrain map elevation variance: The terrain map elevation variance captures the spread of terrain elevations around the mean.

$$\sigma^2 = \frac{1}{N}\sum_{i=1}^{N}(z_i - \mu)^2 \tag{3.33}$$

Terrain map minimum elevation: The terrain map minimum elevation corresponds to the lowest terrain height within the tile.

$$z_{\min} = \min_i(z_i) \tag{3.34}$$

Terrain map maximum elevation: The terrain map maximum elevation corresponds to the highest terrain height within the tile.

$$z_{\max} = \max_i(z_i) \tag{3.35}$$

Terrain map elevation range: Elevation range measures total vertical relief within the tile.

$$z_{range} = z_{\max} - z_{\min} \tag{3.36}$$

Terrain map inter quartile range (IQR): IQR quantifies the spread of the middle 50% of elevation values, reducing sensitivity to outliers.

$$\mathrm{IQR} = Q_{75} - Q_{25} \tag{3.37}$$

Terrain map FFT radial spectral entropy: This feature quantifies the entropy of radially averaged frequency components.

$$H_f = -\sum_k p_k \log p_k \tag{3.38}$$

Terrain map FFT maximum spectral power: Maximum spectral power captures the strongest frequency component magnitude.

$$P_{\max} = \max_{k} P(f_k) \tag{3.39}$$

Terrain map FFT mean spectral power: Mean spectral power represents average frequency-domain energy.

$$\bar{P} = \frac{1}{K}\sum_{k} P(f_k) \tag{3.40}$$

Terrain map FFT median spectral power: Median spectral power is less sensitive to extreme spectral peaks.

$$P_{\text{median}} = \text{median}(P(f_k)) \tag{3.41}$$

Terrain map FFT spectral power standard deviation: This feature measures the variability of spectral energy distribution.

$$\sigma_P = \sqrt{\frac{1}{K}\sum_{k}(P(f_k) - \bar{P})^2} \tag{3.42}$$

3.5.3 Score map–based features

The last group includes features derived from the TERCOM comparison surface, namely the score map. These features include mean, variance, skewness, kurtosis, minima counts, the ratio of the two best minima (minima ratio), and entropy, which together characterize the statistical structure and distinctiveness of the matching surface.

Minima ratio: Minima ratio is a score map–based descriptor that quantifies the distinctiveness of the best candidate solution by comparing the two strongest spatially non-adjacent minima. By focusing on genuinely competing location hypotheses, it provides a direct confidence indicator for TERCOM-based navigation fixes and plays a central role in the false-fix elimination strategy adopted in this study, with further details given in Section 4.3.

Score map mean slope: Mean slope of the score map quantifies the average gradient magnitude of the similarity surface, reflecting how rapidly matching scores change across neighboring candidate positions.

$$\bar{s}_S = \frac{1}{N}\sum_{i=1}^{N}\sqrt{\left(\frac{\partial S}{\partial x}\right)^2 + \left(\frac{\partial S}{\partial y}\right)^2} \tag{3.43}$$

Score map mean planar curvature: Mean planar curvature describes the curvature of the score map perpendicular to the gradient direction, indicating lateral spreading or focusing of score variations.

$$k_{p,S} = \frac{\partial^2 S}{\partial x^2} + \frac{\partial^2 S}{\partial y^2} \tag{3.44}$$

Score map mean profile curvature: Mean profile curvature represents the curvature of the score map along the direction of steepest descent, characterizing the sharpness of minima regions.

$$k_{pr,S} = \frac{\partial^2 S}{\partial s^2} \tag{3.45}$$

Score map skewness: Skewness measures the asymmetry of the score value distribution within the score map.

$$\text{Skewness}_S = \frac{1}{N\sigma_S^3} \sum_{i=1}^{N} (S_i - \mu_S)^3 \tag{3.46}$$

Score map kurtosis: Kurtosis characterizes the peakedness of the score map distribution, highlighting the presence of sharp minima or heavy tails.

$$\text{Kurtosis}_S = \frac{1}{N\sigma_S^4} \sum_{i=1}^{N} (S_i - \mu_S)^4 \tag{3.47}$$

Score map entropy: Entropy quantifies the randomness of score values across the map, where low entropy indicates a more structured and distinctive matching surface.

$$H_S = -\sum_k p_k \log p_k \tag{3.48}$$

Score map mean: Mean score represents the average similarity value across the score map.

$$\mu_S = \frac{1}{N} \sum_{i=1}^{N} S_i \tag{3.49}$$

Score map variance: Score map variance measures the dispersion of score values around the mean within the score map.

$$\sigma_S^2 = \frac{1}{N} \sum_{i=1}^{N} (S_i - \mu_S)^2 \tag{3.50}$$

Score map minimum: The minimum score corresponds to the best-matching candidate position within the score map.

$$S_{\min} = \min_i (S_i) \tag{3.51}$$

Score map maximum: The maximum score corresponds to the worst-matching candidate position within the score map.

$$S_{\max} = \max_i(S_i) \tag{3.52}$$

Score map range: Score range quantifies the spread between the best and worst matching scores across the entire search region.

$$\mathrm{S}_{range} = S_{\max} - S_{\min} \tag{3.53}$$

Score map inter quartile range (IQR): Inter quartile range measures the dispersion of the middle 50% of score values, reducing sensitivity to extreme outliers.

$$\mathrm{IQR}_S = Q_{75,S} - Q_{25,S} \tag{3.54}$$

Score map FFT bandwidth: Bandwidth measures the spread of spectral energy around the centroid in the score map spectrum.

$$\mathrm{BW}_S = \sqrt{\frac{\sum_k (f_k - C_S)^2 P_S(f_k)}{\sum_k P_S(f_k)}} \tag{3.55}$$

Score map FFT spectral entropy: Spectral entropy quantifies the uniformity of frequency-domain energy distribution in the score map.

$$H_{f,S} = -\sum_k p_{k,S} \log p_{k,S} \tag{3.56}$$

Score map FFT maximum spectral power: This feature represents the strongest frequency component magnitude in the score map spectrum.

$$P_{\max,S} = \max_k P_S(f_k) \tag{3.57}$$

Score map FFT mean spectral power: Mean spectral power corresponds to the average energy across frequency components.

$$\bar{P}_S = \frac{1}{K} \sum_k P_S(f_k) \tag{3.58}$$

Score map FFT median spectral power: Median spectral power reduces sensitivity to dominant frequency peaks.

$$P_{\mathrm{median},S} = \mathrm{median}(P_S(f_k)) \tag{3.59}$$

Score map FFT spectral power standard deviation: This feature measures variability in spectral energy distribution of the score map.

$$\sigma_{P,S} = \sqrt{\frac{1}{K}\sum_k (P_S(f_k) - \bar{P}_S)^2} \tag{3.60}$$

3.6 Redundancy Analysis and Feature Elimination

Due to a wide variety of features, significant redundancy was expected, since many terrain metrics were either mathematically or conceptually related to each other. For instance, terrain variance, range, and standard deviation are inherently correlated, while indices such as the TRI and TPI usually have correlation with slope-based features. Including such interdependent features would not only increase the dimension but also reduce interpretability and classifier stability.

To eliminate this problem, a multi-stage feature screening procedure was employed as combining correlation filtering, mutual information (MI) ranking, cross-validated mean area under curve (AUC), and minimum redundancy maximum relevance (mRMR) analysis. First, pairwise Pearson correlations were computed among all 45 features, and whenever two features exhibited a correlation magnitude above 0.80, the one with lower predictive utility (measured AUC) was discarded. Next, the remaining features were ranked by their mutual information with respect to the navigation error label (error < 90 m vs. error ≥ 90 m), and those in the bottom quartile (0.15 as a number without normalization) were removed to eliminate variables with negligible relevance. Subsequently, variables with a cross-validated mean AUC below 0.50 were eliminated. Finally, the features with the lowest 2 nRMR were removed. The overall progression of this elimination pipeline, including the number of features removed and retained at each stage, is summarized in Table 3.1.

Table 3.1: Stepwise screening summary of 45 candidate features.

Stage	Criterion	Removed	Remaining
Start	–	–	45
Redundancy	$\lvert r_{\text{Pairwise}} \rvert \geq 0.80$ (keep higher AUC)	27	18
Relevance	MI < 0.15	7	11
Predictivity	AUC < 0.50	5	6
Relevance + Redundancy	mRMR < 0.02	2	4

After screening, only four features shown in Table 3.2 remained consistently informative. The first one is the minima ratio the strongest predictor, directly linked to false-fix distinctiveness. Second one is score map entropy, as the name suggests, is the entropy of the resulting score map. Third and fourth ones are trajectory roughness and roughness difference, capturing the effect of terrain variability on matching reliability.

Table 3.2: Retained features after screening.

Feature	**Group**	max **Pairwise** $\|r\|$	**MI**	**AUC**	**mRMR**
Minima Ratio	Score map	–	0.550	0.891	0.175
Score Map Entropy	Score map	–	0.300	0.669	0.099
Roughness	Trajectory	0.972	0.228	0.559	0.021
Roughness Difference	Trajectory	0.972	0.276	0.526	0.014

Feature minima ratio, which integrates score-map information, emerge as the most powerful indicator. Score map entropy is other powerful indicator, however minima ratio already carries information about score map and computing the entropy of whole score map is much costly than computing minima ratio. For these reasons it is less suitable for real-time applications and the entropy metric was not investigated. Roughness alone passed these tests, but the roughness difference, which has a very high correlation with roughness, did not. However, since studies [5,6,13,18] have declare that the roughness difference is a metric as important as roughness, both metrics were retained and examined.

4. METHODOLOGY

4.1 Score Map Construction

Based on the comparative analysis in Section 3.4, two score maps are constructed for each comparison metric: one using MAD and the other using DTW. These maps are generated by evaluating the respective comparison function at every candidate position within the search region, where the measured radar altimeter profile is aligned against the terrain derived profile from the DTED database. The MAD-based map emphasizes robustness to noise by penalizing absolute deviations, while the DTW-based map accommodates local misalignment in the altitude sequence by dynamically adjusting the alignment path. As a result, the two score maps provide complementary perspectives on the similarity between the measured and reference profiles. Each pixel on the score map corresponds to a potential location estimate. Lower values indicate a better match. Identifying minima on maps using matching metrics provides preparation for ratio-based reliability assessment and subsequent merging strategies.

4.2 Receiver Operating Characteristic (ROC) Curve Analysis

Decision thresholds were examined, and the resulting correct and incorrect ratios were analyzed. ROC analysis was performed. This allowed for the justification of the cumulative bad/good (B/G) ratio. The resulting ROC curve is shown in Figure 4.1. The diagonal shown in the image is the random classifier, and the resulting ROC curve is located to the left of this diagonal. This demonstrates that the proposed confidence logic has a discriminatory ability beyond random behavior. Specifically, B/G values of 1 and 5 correspond to operating points that achieve high true positive rates of approximately 95% and 99%, respectively. B/G = 2 was chosen as an intermediate reference point to represent a balanced operating regime. Therefore, these thresholds correspond to representative operating points near the upper left region of the ROC curve. Instead of focusing on a single global optimal threshold, this study also examined different trade-offs between false-fix suppression and update availability.

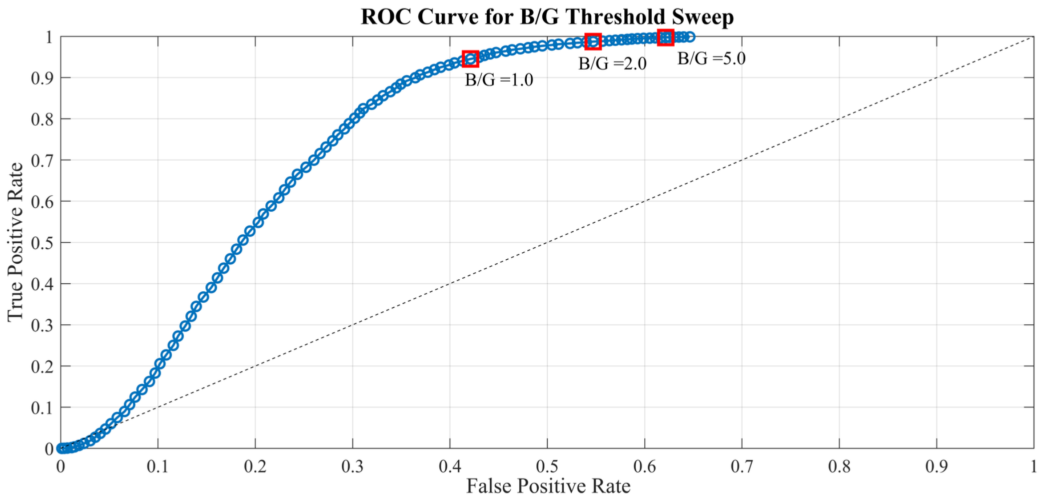

Figure 4.1: ROC Curve for corresponding B/G thresholds.

ROC curve obtained by sweeping the B/G decision threshold. Selected thresholds (B/G = 1, 2, and 5) are highlighted as representative operating points corresponding to different trade-offs between true positive rate and false positive rate.

4.3 Minima Identification and Ratio Test

From each score map, the two most prominent minimas (best and second-best candidates) are extracted. To prevent redundancy, only minimas that are spatially distinct are considered. Then the distinctiveness of the best candidate relative to the second-best evaluated by computing the minima ratio, defined as:

$$R = \begin{cases} 0, & \text{if } \mathrm{Score}_{\mathrm{second}} = 0 \\ \frac{|\mathrm{Score}_{\mathrm{best}} - \mathrm{Score}_{\mathrm{second}}|}{\mathrm{Score}_{\mathrm{second}}} \times 100, & \text{else} \end{cases} \tag{4.1}$$

This normalized ratio measures how clearly the best candidate stands out from competing alternatives. The histogram of minima ratio and navigation error is given in Fig. 4.2. This ratio is computed independently for both MAD and DTW maps, providing two complementary confidence assessments. To empirically determine a suitable limit, cumulative bad-to-good (B/G) ratio thresholds were analyzed, each defining the relative density of false to correct fixes. To identify stable breakpoints and measure sensitivity, these threshold values were tested on the dataset. A small minima ratio indicates that candidate positions are equally likely, while a high ratio indicates that a candidate position is much more likely. The reliability of the solutions is also related to this.

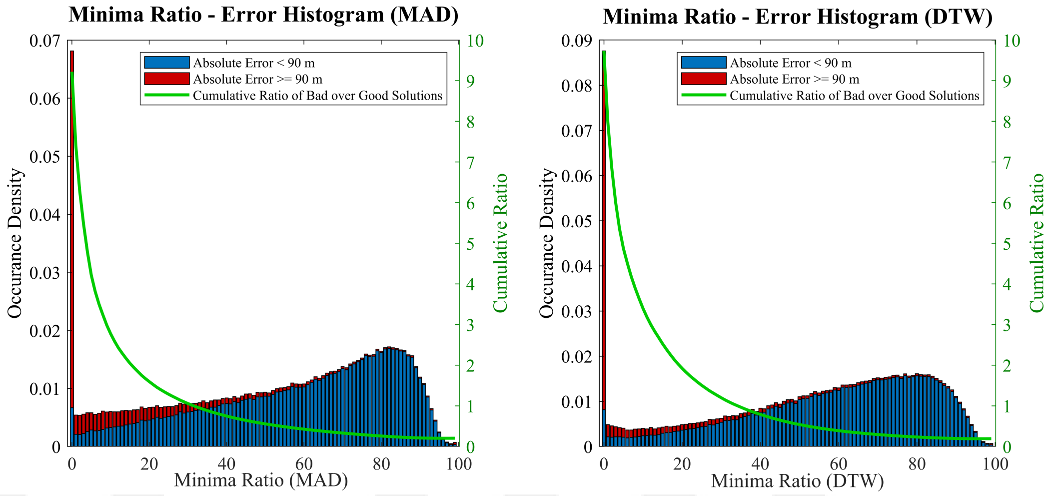

Figure 4.2: Histogram of minima ratio and navigation error.

4.4 Score Map Combination Strategy

Experimental results showed that the MAD and DTW metrics did not always produce the same predictions. That is, they yielded different predictions in different situations. This is actually expected, as MAD focuses on the linear similarity of sequences, while DTW is tolerant of local alignment errors between sequences. Therefore, they encompass different and complementary features.

It has been suggested to leverage these complementary features using a minima-ratio-based selection strategy. A larger ratio indicates a more significant minima and a more reliable match. Therefore, instead of combining metrics, the metric with the largest minima-ratio value among the candidate solutions, i.e., the more reliable metric, was selected. This enables an adaptive selection mechanism that selects the metric providing the clearer separation between competing prediction.

The position hypothesis (PRO) is selected from either MAD or DTW according to which score map exhibits the larger minima ratio. Formally, where R_k is the minima ratio of metric k and $C_k(\mathbf{x})$ is its comparison map.

$$k^\star = \arg \max_{k \in \{\mathrm{MAD}, \mathrm{DTW}\}} R_k \tag{4.2}$$

$$(\mathbf{x}, \mathbf{y})_{\mathrm{PRO}} = \arg \min_{\mathbf{x}, \mathbf{y}} C_{k^\star}(\mathbf{x}, \mathbf{y}) \tag{4.3}$$

Error distribution graphs for these three metrics —MAD, DTW, and PRO— are shown in Fig. 4.3. This simple yet effective rule significantly reduces the occurrence of false fixes across various test conditions. The predicted solution's false-fix rates are 0.098, 0.123, and 0.091, respectively. In other words, combining the metrics relatively improved the false-fix rate by 7.14% and 26.02%, respectively.

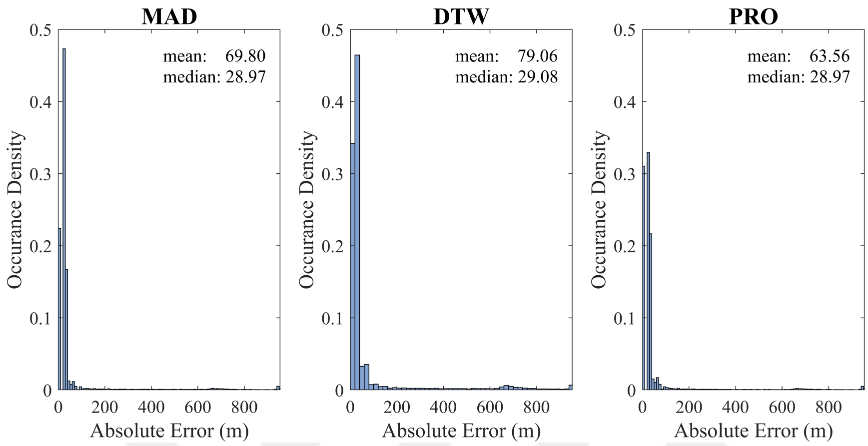

Figure 4.3: Navigation error comparisons of MAD, DTW and PRO.

4.5 Roughness and Roughness Difference Test

Path height standard deviation σ_T (called roughness) and path height slope standard deviation σ_Z (called roughness difference) parameters are examined. N is the number of samples, h_i is the terrain height measurement, and $\overline{h}$ is the mean height of that terrain. These parameters capture the geometric variability of the terrain profile along the flight path and provide an indication of terrain distinctiveness.

$$\overline{h} = \frac{1}{N}\sum_{i=1}^{N} h_i \tag{4.4}$$

By using h_i and $\overline{h}$ path height standard deviation σ_T can be calculated as below.

$$\sigma_T = \sqrt{\frac{1}{N}\sum_{i=1}^{N}(h_i - \overline{h})^2} \tag{4.5}$$

In order to calculate the path height slope standard deviation σ_Z, slopes d_i should be found first and $\overline{d}$ is the mean of the slopes.

$$d_{i-1} = h_{i-1} - h_i \tag{4.6}$$

$$\overline{d} = \frac{1}{N-1}\sum_{i=1}^{N-1} d_i \tag{4.7}$$

By using d_i and $\overline{d}$ path height slope standard deviation σ_Z can be calculated as below.

$$\sigma_Z = \sqrt{\frac{1}{N-1}\sum_{i=1}^{N-1}(d_i - \overline{d})^2} \tag{4.8}$$

Histogram of roughness, roughness difference, and navigation error are given in Fig. 4.4. Increasing terrain roughness and slope variability correlate with reduced navigation error. While the discrimination is not obvious in moderate and high roughness situations, these features become quite distinctive in very low roughness situations. Similarly, the cumulative ratio was examined for these and the base thresholds for the tests were selected where the cumulative B/G ratio was 5, 2, and 1.

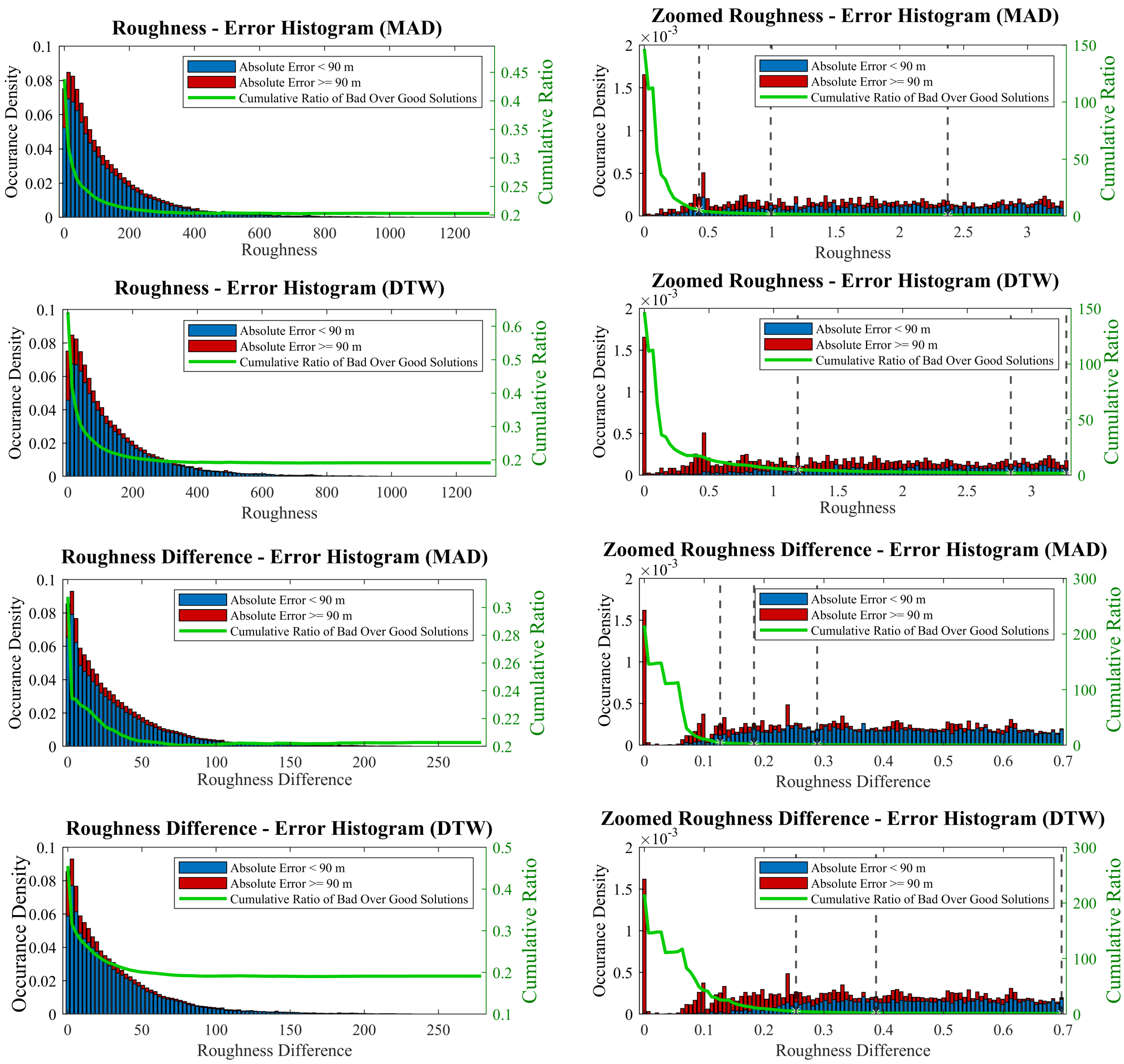

Figure 4.4: Histogram of roughness and roughness difference over navigation error.

4.6 Elimination and Confidence Categorization

After constructing the MAD and DTW score maps, their respective minima ratios were computed for each navigation window. The algorithm first compares these two ratios and selects the metric (MAD or DTW) that exhibits the higher ratio as the candidate solution, ensuring that the most distinctive score map guides the final decision. The analysis was conducted by testing thresholds for the minima ratio, roughness, and roughness difference, in accordance with the mentioned B/G ratio. Fig. 4.5 demonstrates the corresponding precision, recall, accuracy, and false-fix values. As expected, as the threshold increases, the recall value and false-fix rate decrease, while precision increases to a certain extent. Since accuracy is a measure of correct decisions and as the threshold value increases, abstain decisions are made in every situation, accuracy tends to decrease. The primary goal here is to reduce the false-fix rate without significantly decreasing recall.

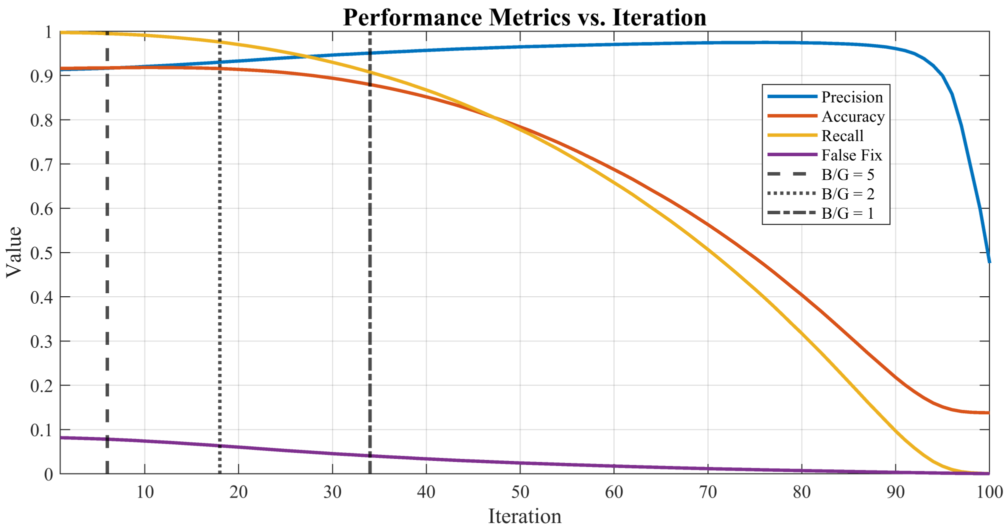

Figure 4.5: Precision, recall, accuracy, false-fix rate over different B/G ratio thresholds.

Given thresholds are for B/G ratios equal to 5, 2, and 1, respectively.

$$\begin{gathered} R_{\text{MAD}} < 4, \quad \sigma_{T,MAD} < 0.4, \quad \sigma_{Z,MAD} < 0.13 \\ R_{\text{DTW}} < 5, \quad \sigma_{T,DTW} < 1.2, \quad \sigma_{Z,DTW} < 0.25 \end{gathered} \tag{4.9}$$

$$\begin{gathered} R_{\text{MAD}} < 15, \quad \sigma_{T,MAD} < 1.0, \quad \sigma_{Z,MAD} < 0.18 \\ R_{\text{DTW}} < 19, \quad \sigma_{T,DTW} < 2.8, \quad \sigma_{Z,DTW} < 0.39 \end{gathered} \tag{4.10}$$

$$\begin{gathered} R_{\text{MAD}} < 32, \quad \sigma_{T,MAD} < 2.4, \quad \sigma_{Z,MAD} < 0.29 \\ R_{\text{DTW}} < 34, \quad \sigma_{T,DTW} < 3.3, \quad \sigma_{Z,DTW} < 0.70 \end{gathered} \tag{4.11}$$

If any of these conditions is satisfied, the algorithm raises an *abstain* flag, indicating an unreliable solution excluded from the navigation update. Otherwise, a *fix* flag is issued for position correction. To evaluate the sensitivity of this logic, the ratio thresholds were tested under three (B/G) ratios of 5, 2, and 1. The distributions of the confusion matrix elements were tested for each test value, and the results are shown in Figure 4.6. These elements correspond, respectively, to correct correction acceptance, correct avoidance, missed corrections, and undetected incorrect corrections. This framework allows for the examination of the trade-off between safety and solution continuity based on threshold selection.

In all experiments, the evaluation criterion for a *good* fix was defined as position error less than 90 m, consistent with the DTED-2 horizontal resolution ($\sigma = 30$m) and a 3σ tolerance band adopted throughout this study. Consequently, the *fix* category represents cases where the position estimation error is less than 90 meters.

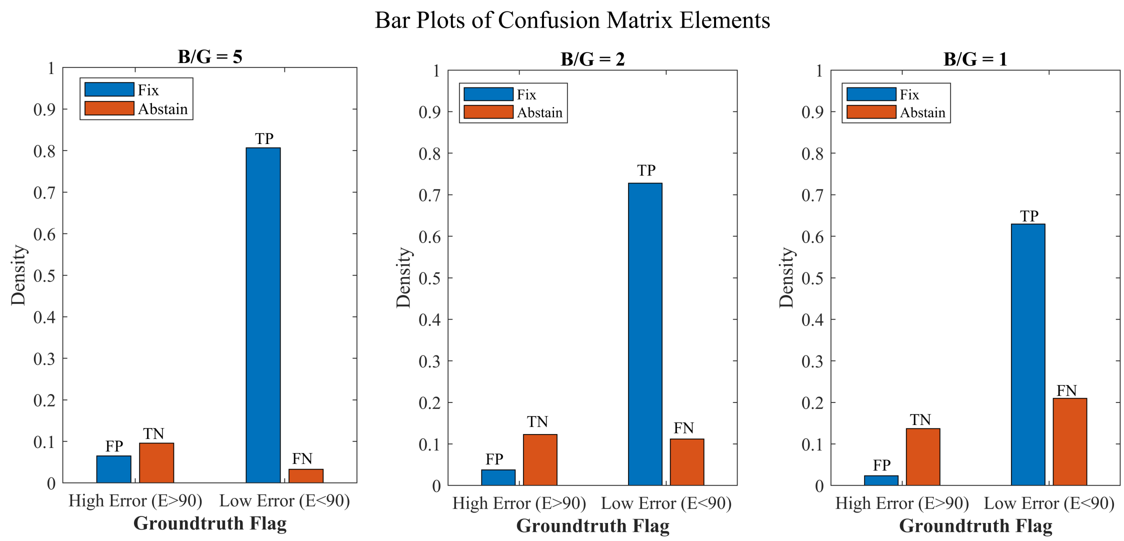

Figure 4.6: Bar plots of confusion matrix elements for three cumulative bad-to-good (B/G) ratios of 5, 2, and 1. Each subfigure compares the density of true positives (TP), true negatives (TN), false positives (FP), and false negatives (FN) under different ratio thresholds, demonstrating the effect of reliability criteria on fix and abstain decisions.

5. RESULTS AND DISCUSSION

To validate the proposed false-fix elimination framework, the algorithm is tested with real Flight Test Instrumentation (FTI) data acquired from the Hürjet advanced jet trainer platform. The dataset was sampled at 128 Hz, while the TERCOM algorithm operated at 20 Hz. Three navigation solutions were available during the flights: the free-inertial (FI) solution, the GNSS solution, and the hybrid (filtered GNSS–INS) solution. Since the hybrid solution provides the most accurate navigation performance, it was adopted as the ground truth for evaluating results. Radar-altimeter measurements are generated as explained in the Sec. 3.5. Since radalt measurements would be less accurate during high roll or yaw maneuvers, the tests were conducted for wings-level flights. This ensured that the analysis realistically represented operational flight conditions.

Error and uncertainty metrics were defined in the same way as metrics in our previous work [1,26]. e_{x_i} and e_{y_i} are the position errors between the ground truth and the predicted position. By taking the mean of these absolute errors, mean absolute error (MAE) is calculated.

$$\mathbf{Error}_i = \sqrt{e_{x_i}^2 + e_{y_i}^2} \tag{5.1}$$

Positional uncertainty is defined with the circular error probable (CEP) metric. The standard deviations of the position errors between the ground truth, and the prediction is denoted as σ_x and σ_y. Also, μ_x and μ_y are the means of the position errors. CEP is calculated by using calculated coefficient and means.

$$\mathbf{C}_0 = \begin{cases} 0.562\sigma_x + 0.615\sigma_y, & \sigma_y < \sigma_x \text{ and } \frac{\sigma_y}{\sigma_x} < 0.28 \\ 0.562\sigma_y + 0.615\sigma_x, & \sigma_x < \sigma_y \text{ and } \frac{\sigma_x}{\sigma_y} < 0.28 \\ 1.1774\frac{(\sigma_x+\sigma_y)}{2}, & \text{else} \end{cases} \tag{5.2}$$

$$CEP = \sqrt{C_0^2 + \mu_x^2 + \mu_y^2} \tag{5.3}$$

An experiment was performed with 1500 seconds. The results for INS, MAD, DTW and the proposed algorithm with B/G selected as 2 are given in Table 5.1. The mean error of INS is large because it drifts with time during long flights. Based on this information, the proposed algorithm provides accuracy improvements of 20%, and 46% over MAD, and DTW, respectively. Furthermore, the number of false fixes are decreased to 16 from 29 and 75 respectively. The results clearly indicate that the algorithm has achieved significant improvement.

Table 5.1: MAE results with real flight test instrumentation data

Method	MAE (m)	CEP (m)	F-F
FI	*505.72*	*536.98*	-
MAD	*35.98*	*65.83*	*29*
DTW	*53.51*	*102.71*	*75*
Proposed	**28.92**	**43.36**	**16**

Fig. 5.1 and Fig. 5.2 illustrates the absolute position error over time for two representative 150-seconds flight segments. As a reference, B/G selected as 2. As expected, the FI solution exhibits progressive drift. The MAD-based and DTW-based TERCOM algorithms periodically corrects the position, but sometimes introduce dramatic false fixes. Proposed combination and elimination strategy successfully detects and mitigates these errors.

For first flight test demonstrated in Fig. 5.1, DTW introduced false fixes with large error, and MAD yielded relatively more accurate solution. Moreover, the proposed method detected the large false fixes and generally chose the more accurate solution.

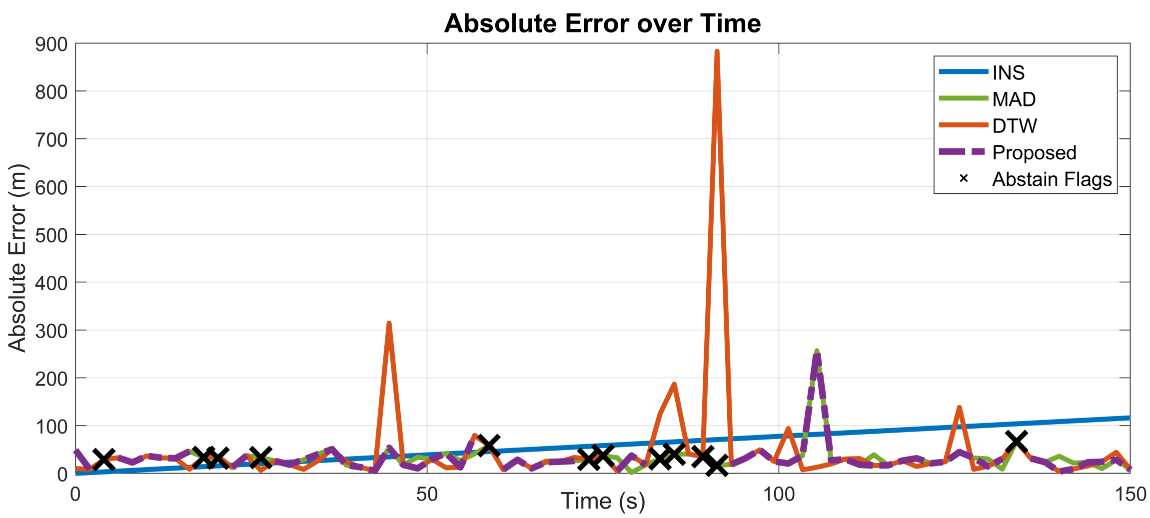

Figure 5.1: Absolute navigation error over time plot with FTI data.

For second flight test shown in Fig. 5.2, in contrary of the first flight, MAD introduced false fixes with large error, and DTW gives more accurate solution. Similarly, the proposed method successfully detected the large false fixes and generally chose the low error solution.

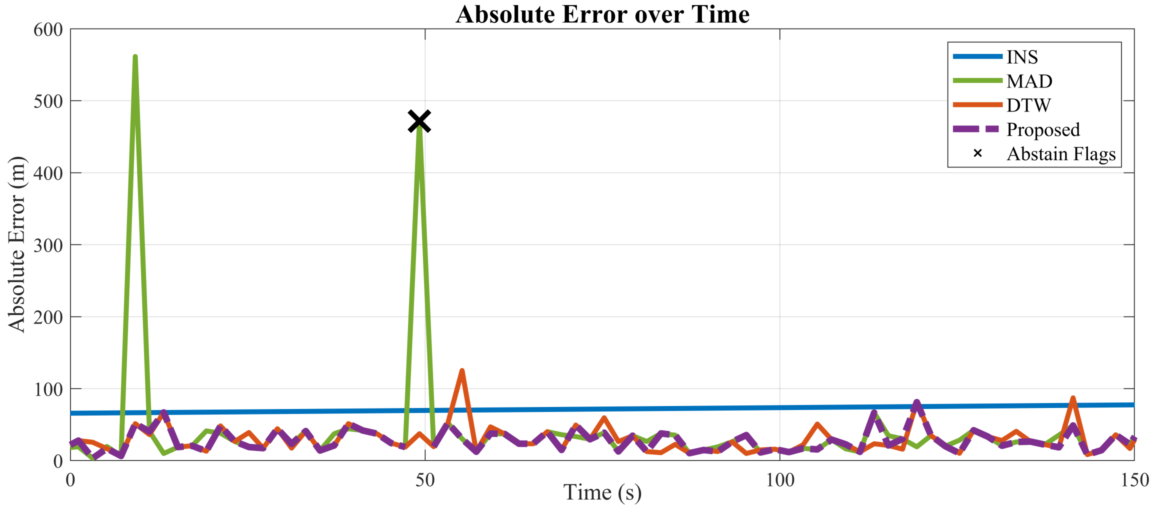

Figure 5.2: Absolute navigation error over time plot with FTI data.

Numeric results for these two flights are summarized in Table 5.2. The suggested approach enhances performance in terms of MAE, CEP, and false-fix, as this table demonstrates.

Table 5.2: Results of tests on real flight test instrumentation data

	1st Flight Test			**2nd Flight Test**		
Method	**MAE (m)**	**CEP (m)**	**F-F**	**MAE (m)**	**CEP (m)**	**F-F**
FI	*65.77*	*72.12*	-	*80.25*	*87.27*	-
MAD	*31.72*	*38.02*	*1*	*39.98*	*75.19*	*2*
DTW	*45.64*	*97.81*	*5*	*30.00*	*31.44*	*2*
Proposed	**30.86**	**37.79**	**1**	**27.97**	**29.13**	**0**

In conclusion, results from flight-test evaluations consistently show that by incorporating a statistical reliability check, the proposed approach enhances TERCOM's robustness under diverse terrain conditions without requiring additional sensors or major architectural changes. Tests conducted on the Hürjet confirm the feasibility of the proposed algorithm for GNSS-denied operations on advanced jet training aircraft platforms.

6. CONCLUSIONS

This study focuses on a statistical framework that enhances the robustness of the TERCOM algorithm used in GNSS-denied environments. The proposed framework enables a low-computational matching reliability classification using features generated during comparison. This method effectively identifies and eliminates false-fixes that occur during TERCOM matching.

The framework was created using synthetic trajectories generated from Hürjet's real FTI records. Various features were extracted from these trajectories, and classification was considered appropriate using minima ratio, roughness, and roughness difference. Furthermore, since MAD and DTW matching metrics were both successful and complementary, these two metrics were combined with the selected features. Classification was then performed according to specific thresholds to detect false-fixes.

Compared to traditional TERCOM, the proposed elimination-based algorithm achieved a reduction in MAE, CEP, and false-fixes. This reduction was achieved without incurring a significant computational load, as the features already generated during the calculation is used. This provides an adaptable false-fix protection for avionics systems with limited computational capabilities that need to operate in real time.

REFERENCES

[1] **Bekar, Ü.C.**, **Tanyeri, B.**, **Uslu, I.E.**, **Gungor, N.A. and Inalhan, G.** (2025). Validation of an AI-Assisted Terrain-Aided Navigation Algorithm Using Real-World Flight Test Instrumentation Data, *Aerospace*, *12*(6), 501.

[2] **Golden, J.P.** (1980). Terrain contour matching (TERCOM): a cruise missile guidance aid, *Image processing for missile guidance*, volume238, SPIE, pp.10–18.

[3] **Carr, J.R. and Sobek, J.S.** (1980). Digital scene matching area correlator (DSMAC), *Image Processing For Missile Guidance*, volume238, SPIE, pp.36–41.

[4] **Hostetler, L.D. and Andreas, R.** (1983). Nonlinear Kalman filtering techniques for terrain-aided navigation, *IEEE Transactions on Automatic Control*, *28*(3), 315–323.

[5] **Yoo, Y.**, **Lee, W.**, **Lee, S.**, **Park, C. and Kwon, J.** (2012). Improvement of TERCOM aided inertial navigation system by velocity correction, *Proceedings of the 2012 IEEE/ION Position, Location and Navigation Symposium*, IEEE, pp.1082–1087.

[6] **Wei, E.**, **Dong, C.**, **Yang, Y.**, **Tang, S.**, **Liu, J.**, **Gong, G. and Deng, Z.** (2017). A robust solution of integrated SITAN with TERCOM algorithm: weight-reducing iteration technique for underwater vehicles' gravity-aided inertial navigation system, *NAVIGATION: Journal of the Institute of Navigation*, *64*(1), 111–122.

[7] **Zhao, L.**, **Gao, N.**, **Huang, B.**, **Wang, Q. and Zhou, J.** (2014). A novel terrain-aided navigation algorithm combined with the TERCOM algorithm and particle filter, *IEEE Sensors Journal*, *15*(2), 1124–1131.

[8] **Wu, L.**, **Wang, H.**, **Chai, H.**, **Hsu, H. and Wang, Y.** (2015). Research on the relative positions-constrained pattern matching method for underwater gravity-aided inertial navigation, *The Journal of Navigation*, *68*(5), 937–950.

[9] **Kadri, M.B. and Yousuf, S.** (2025). An advanced error state Kalman filter (ESKF)-based terrain contour matching (TERCOM) method for tracking an aerial vehicle using a low-cost digital elevation map, *PeerJ Computer Science*, *11*, e3118.

[10] **Chang, Y.**, **Wang, R. and Zhou, X.** (2025). Research on Improving the Joint Matching Algorithm Between TERCOM and ICP, *2025 5th International*

Conference on Mechanical, Electronics and Electrical and Automation Control (METMS), IEEE, pp.519–524.

[11] **Peng, H.Z.**, **Jun, Y.**, **Wei, W.W. and Zhi, M.B.** (2018). An algorithm of terrain matching Aided Navigation for UAVs, *2018 IEEE CSAA Guidance, Navigation and Control Conference (CGNCC)*, IEEE, pp.1–6.

[12] **Wei, F.**, **Yuan, Z. and Zhe, R.** (2015). UKF-Based Underwater Terrain Matching Algorithms Combination, *2015 International Industrial Informatics and Computer Engineering Conference*, Atlantis Press, pp.1027–1030.

[13] **Ekütekin, V.** (2007). *Navigation and control studies on cruise missiles*, Middle East Technical University (Turkey).

[14] **Jarraya, I.**, **Abdelkader, M.**, **Gabr, K.**, **AlMusalami, A.**, **Kadri, M.B. and Koubaa, A.** (2024). Non-visual Terrain Navigation for UAVs: A Comparative Study in GPS-Denied Environments, *International Conference on Smart Systems and Emerging Technologies*, Springer, pp.345–357.

[15] **Carroll, J.D. and Canciani, A.J.** (2021). Terrain-referenced navigation using a steerable-laser measurement sensor, *Navigation*, *68*(1), 115–134.

[16] **Cheng, S.**, **Wang, H.**, **Ji, H. and Li, D.** (2017). Design of UAV distributed aided navigation simulation system based on scene/terrain matching, *2017 11th Asian Control Conference (ASCC)*, IEEE, pp.360–364.

[17] **Cowie, M.**, **Wilkinson, N. and Powlesland, R.** (2008). Latest development of the terprom® digital terrain system (dts), *2008 IEEE/ION Position, Location and Navigation Symposium*, IEEE, pp.1219–1229.

[18] **Wang, K.**, **Zhu, T.**, **Qin, Y.**, **Jiang, R. and Li, Y.** (2018). Matching error of the iterative closest contour point algorithm for terrain-aided navigation, *Aerospace Science and Technology*, *73*, 210–222.

[19] **Naik Bhukya, R.**, **Kodepaka, S.**, **Dharavath, V. and Boda, R.** (2020). Position and Velocity Errors Reduction Using Advanced TERCOM Aided Inertial Navigation System, *International Conference on Innovative Computing and Communications: Proceedings of ICICC 2020, Volume 1*, Springer, pp.801–809.

[20] **Shuai, X.**, **Wu, S.C. and Luo, N.B.** (2014). The Dynamic TERCOM Algorithm of Underwater Positioning Based on Terrain Entropy, *Applied Mechanics and Materials*, *644*, 1774–1777.

[21] **Liu, Y. and Tan, Z.f.** (2011). Research and Design of Terrain Aided Navigation System, *2011 7th International Conference on Wireless Communications, Networking and Mobile Computing*, IEEE, pp.1–4.

[22] **Sineglazov, V.** (2014). Main features of terrain-aided navigation systems, *2014 IEEE 3rd International Conference on Methods and Systems of Navigation and Motion Control (MSNMC)*, IEEE, pp.49–52.

[23] **Lee, S. and Bang, H.** (2018). Terrain contour matching with recurrent neural networks, *2018 IEEE Aerospace Conference*, IEEE, pp.1–9.

[24] **Chen, P.**, **Li, Z.**, **Liu, G.**, **Wang, Z.**, **Chen, J.**, **Shi, S.**, **Shen, J. and Li, L.** (2024). Underwater Terrain Matching Method Based on Pulse-Coupled Neural Network for Unmanned Underwater Vehicles, *Journal of Marine Science and Engineering*, *12*(3), 458.

[25] **Guan, T.**, **Zhang, G. and Chen, P.** (2021). A terrain matching navigation algorithm for UAV, *2021 33rd Chinese Control and Decision Conference (CCDC)*, IEEE, pp.5203–5207.

[26] **Bekar, U.C.**, **Tanyeri, B.**, **Canoglu, A.S.**, **Uslu, I.E.**, **Gungor, N.A. and Inalhan, G.** (2024). AI-assisted Digital Terrain System for an Advanced Jet Trainer, *2024 AIAA DATC/IEEE 43rd Digital Avionics Systems Conference (DASC)*, IEEE, pp.1–10.

[27] **Han, Y.**, **Wang, B.**, **Deng, Z.**, **Wang, S. and Fu, M.** (2017). A mismatch diagnostic method for TERCOM-based underwater gravity-aided navigation, *IEEE Sensors Journal*, *17*(9), 2880–2888.

[28] **Gao, S. and Cai, T.** (2023). A confidence assessment method for positioning errors in gravity-aided navigation, *2023 International Conference on Ocean Studies (ICOS)*, IEEE, pp.007–010.

[29] **Fan, G.**, **Liu, X.**, **Li, Y.**, **Li, J.**, **Han, Y.**, **He, L. and Chen, P.** (2025). A Terrain-Aided Navigation Method Incorporating Terrain Matching and Terrain Suitability Analysis, *IEEE Access*.

[30] **Wang, Q.**, **Gong, X.**, **Bai, X.**, **Deng, Z. and Zhao, S.** (2024). The Method for Selecting Adaptation Zones of Terrain Matching Based on Arctic Seabed Terrain Features, *International Conference on Guidance, Navigation and Control*, Springer, pp.592–601.

[31] **Zhao, S.**, **Zheng, W.**, **Li, Z.**, **Zhu, H. and Xu, A.** (2023). Improving matching efficiency and out-of-domain positioning reliability of underwater gravity matching navigation based on a novel domain-center adaptive-transfer matching method, *IEEE Transactions on Instrumentation and Measurement*, *72*, 1–11.

[32] **Zhao, S.**, **Zheng, W.**, **Li, Z.**, **Zhu, H. and Xu, A.** (2022). Improving matching efficiency and out-of-domain reliability of underwater gravity matching navigation based on a novel soft-margin local semicircular-domain re-searching model, *Remote Sensing*, *14*(9), 2129.

CURRICULUM VITAE

Name SURNAME: Ibrahim Enes Uslu

EDUCATION:

- **B.Sc.:** 2023, Istanbul Technical University, Faculty of Electrical and Electronics Engineering, Electronics and Communication Engineering Department
- **B.Sc.:** 2025, Istanbul Technical University, Faculty of Science and Letters, Physics Engineering Department
- **M.Sc.:** 2026 (Present), Istanbul Technical University, Faculty of Electrical and Electronics Engineering, Telecommuniation Engineering Department

PROFESSIONAL EXPERIENCE AND REWARDS:

- 2023 (Present) Working full-time software engineer in the Avionics Team at TAI
- 2023 Graduated at ISTANBUL Technical University, Electronics and Communication Engineering with highest GPA from department and faculty
- 2022 Started working part-time software engineer in the Avionics Team at TAI
- 2021 Completed the internship in the Health Systems MRI Team at ASELSAN

PUBLICATIONS, PRESENTATIONS AND PATENTS ON THE THESIS:

- Bekar, Ü. C., Tanyeri, B., **Uslu, I. E.**, Gungor, N. A., & Inalhan, G. (2025). Validation of an AI-Assisted Terrain-Aided Navigation Algorithm Using Real-World Flight Test Instrumentation Data. Aerospace, 12(6), 501.
- Bekar, U. C., Tanyeri, B., Canoglu, A. S., **Uslu, I. E.**, Gungor, N. A., ve Inalhan, G. (2024), "AI-assisted Digital Terrain System for an Advanced Jet Trainer," 2024 AIAA DATC/IEEE 43rd Digital Avionics Systems Conference (DASC), San Diego, CA, USA, 2024, ss. 1-10, doi: 10.1109/DASC62030.2024.10749144.

OTHER PUBLICATIONS, PRESENTATIONS AND PATENTS:

- **Uslu, I. E.**, Akkas, A. S., Gulbahce, M. O., & Kocaarslan, I. (2025). Design of Electrodynamic Suspension System for Hyperloop Pod. Turk J Electr Power Energy Syst, 5(2), 125-131.

- **Uslu, İ. E.**, Akkaş, A. S., Gülbahçe, M. O., Özer, K., & Kocaarslan, İ. Hyperloop Kapsülü için Manyetik Askılama Sistemi Tasarımı Design of Magnetic Levitation System for Hyperloop Pod.

- Altıntaş, G., Yasar, H., **Uslu, I. E.**, Demirel, Y., Akinci, M. N., Yilmaz, T., & Akduman, I. (2023). Microwave Antenna Excitation Optimization with Deep Learning For Breast Cancer Hyperthermia. Authorea Preprints.

- Yildiz, G., Yasar, H., **Uslu, I. E.**, Demirel, Y., Akinci, M. N., Yilmaz, T., & Akduman, I. (2022). Antenna excitation optimization with deep learning for microwave breast cancer hyperthermia. Sensors, 22(17), 6343.

- Altintas, G., Yasar, H., **Uslu, I. E.**, Demirel, Y., Joof, S., Akıncı, M. N., ... & Akduman, İ. (2022, July). Antenna Array Optimization via Deep Learning For Breast Cancer Microwave Hyperthermia Application: Preliminary Results. In 2022 IEEE International Symposium on Antennas and Propagation and USNC-URSI Radio Science Meeting (AP-S/URSI) (pp. 697-698). IEEE.